DOI: 10.1002/anie.200700987

Solid-State Reactions

How Is Oxygen Incorporated into Oxides? A Comprehensive Kinetic Study of a Simple Solid-State Reaction with $SrTiO_3$ as a Model Material

Rotraut Merkle and Joachim Maier*

Keywords:
defect chemistry · mixed conductors · oxygen incorporation · perovskites · reaction kinetics

Dedicated to Professor Hermann Schmalzried on the occasion of his 75th birthday

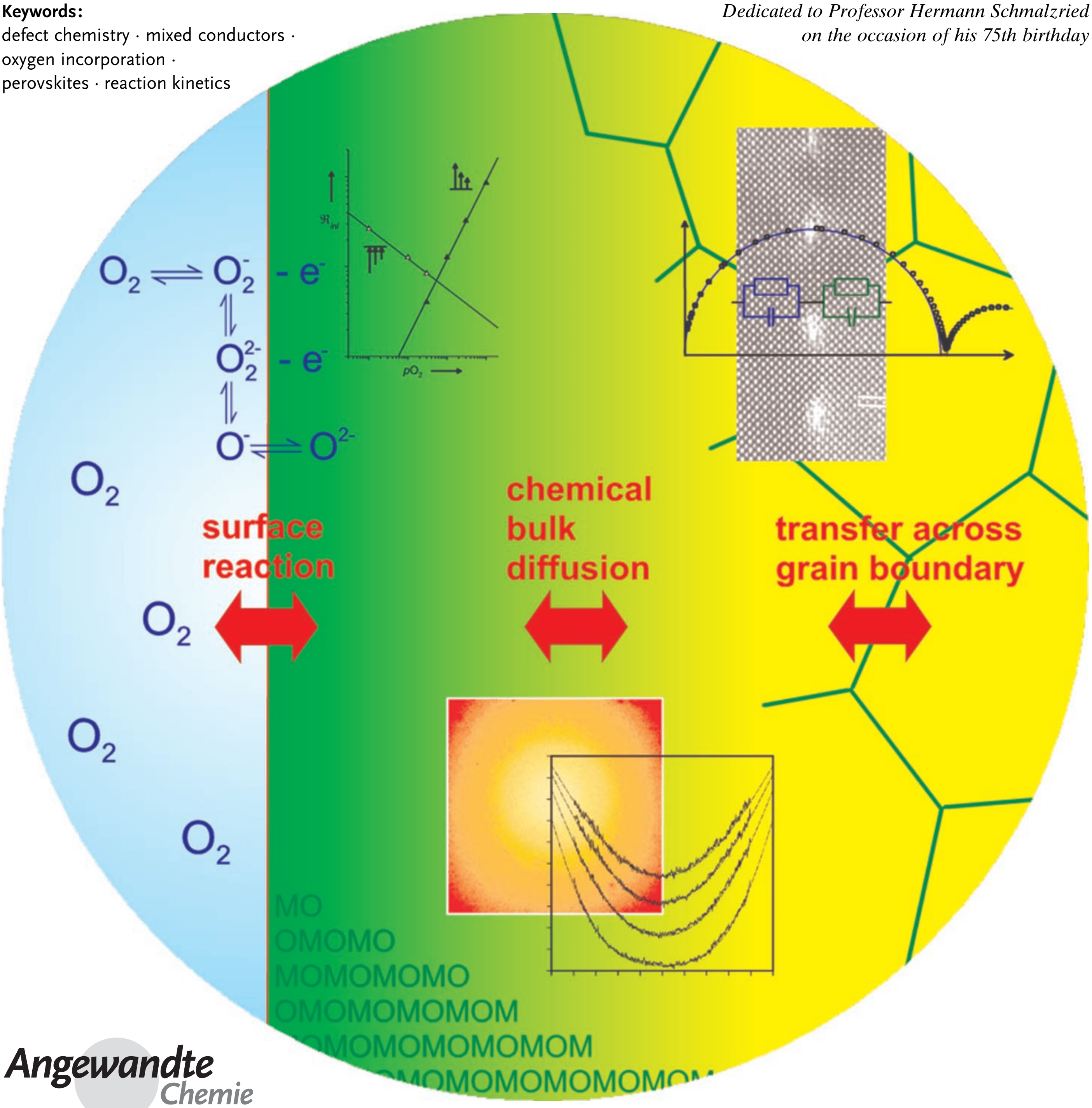

The kinetics of stoichiometry change of an oxide—a prototype of a simple solid-state reaction and a process of substantial technological relevance—is studied and analyzed in great detail. Oxygen incorporation into strontium titanate was chosen as a model process. The complete reaction can be phenomenologically and mechanistically understood beginning with the surface reaction and ending with the transport in the perovskite. Key elements are a detailed knowledge of the defect chemistry of the perovskite as well as the application of a variety of experimental and theoretical tools, many of them evolving from this study. The importance of the reaction and transport steps for (electro)chemical applications is emphasized.

From the Contents

1. Introduction

Owing to the significance of interfaces and the typically sluggish transport, reactions involving solids are much more difficult to describe than reactions between fluid phases. In Germany, the study of solid-state reactions has a significant tradition reaching back to Tammann,[1] Jost,[2] and Wagner,[3,4] and is particularly well treated in H. Schmalzried's book *Solid State Reactions*.[5] The treatment ranges from homogeneous reactions within solids to nonlinear kinetics of complex reactions. The special aspects of interfacial reactions including relevance for heterogeneous catalysis are considered for example, in references [6,7]. Recently, substantial progress was achieved in several respects, for example: 1) in the understanding of elementary chemical reaction steps at gas–solid interfaces;[8–12] 2) in connecting elementary rate constants with effective parameters measured in relaxation kinetics;[13–17] 3) in including space charges into chemical diffusion;[18–20] 4) in taking into account coupling diffusion with internal reactions;[21,22] 5) in the study of complex and nonlinear processes.[23–33] On the experimental front, the development of specific in situ techniques has contributed to the in-depth understanding of defect chemistry and transport (see, for example, references [23,34–37]).

Using strontium titanate as a model material, we had the ambition to understand one of the simplest chemical reactions—namely the incorporation of oxygen into strontium titanate, which does not involve the formation or the motion of interfaces—in great detail ranging from the adsorption of oxygen molecules up to transport of oxygen in the bulk and even across internal boundaries. In spite of the apparent simplicity of the process, its importance as a prototype reaction is enormous. Oxygen incorporation in oxides is an extremely important example of the stoichiometry change of an ionic material. Even when such compositional changes are minute, the effect they have on the "internal chemistry" is always drastic. In other words, the changes occurring when going through the phase width are of first order with respect to internal acid–base and redox chemistry as well as in terms of ionic and electronic charge-carrier densities.

Changes in the oxygen content of about 10 ppm (i.e. a pO_2 change from 10^{-25} to 10^{-5} bar at 800°C) transform SrTiO$_3$ from a good n-type conductor into a poor electronic conductor of p-type. The fine-tuning of oxygen content allows one to switch not only from n- to p-type conductivity[38,39] but also from electronic to ionic[40] conductivity. In mixed conducting materials such as in $Sr(Fe_xTi_{1-x})O_{3-\delta}$,[40] the stoichiometry can be frozen out by rapid quenching of the samples. In the high-temperature superconductor material $YBa_2Cu_3O_{6+\delta}$, the oxygen stoichiometry determines whether the compound is normal conducting or superconducting. In the region around $\delta = 0.5$, a variation of $\Delta\delta = 0.1$ is able to change the critical temperature T_c by 50 K.[41] Magnetic properties such as magnetoresistance (an important quantity for information storage devices) can depend sensitively on oxygen content as demonstrated, for example, for $SrFeO_{3-\delta}$.[42] In this material, the exact δ value also determines the crystallographic structure and can lead to phase changes from an orthorhombic brownmillerite structure to tetragonal or cubic perovskite structures.[43] Oxygen loss at high temperatures (or low pO_2) influences the overall thermal expansion, leading to a pronounced excess "chemical" contribution (e.g. in $Sr(Fe_xTi_{1-x})O_{3-\delta}$[44]), which is undesired in permeation membranes as well as in solid-oxide fuel-cell (SOFC) components.

Oxygen incorporation and extraction processes and their detailed kinetics are crucial for the functioning of many (electro)chemical devices. The following examples may

---

[*] Dr. R. Merkle, Prof. Dr. J. Maier
Max-Planck-Institut für Festkörperforschung
Heisenbergstrasse 1, 70569 Stuttgart (Germany)
Fax: (+49) 711-689-1722
E-mail: sofia.weiglein@fkf.mpg.de
Homepage: http://www.fkf.mpg.de/maier/

suffice: Chemical oxygen incorporation or removal kinetics is decisive for the performance of mixed conducting oxygen permeation membranes,[45] which can either be used for oxygen separation, or for direct oxygen conversion in (partial) oxidation reactions (see reference [46]). Oxygen incorporation is the signal-determining process in bulk conductivity sensors (see for example reference [47]). Even though this is not the case for surface conductivity sensors, the incorporation kinetics determines drift effects in such sensors as well as the selectivity for other redox-active gases (see for example reference [48]). Often, good oxidation catalysts are mixed conductors.[49,50] Their oxygen content may either adjust to the operation conditions merely as a side effect, but the contribution of lattice oxygen can also represent an essential feature of the catalyst's activity and selectivity ("Mars-van-Krevelen mechanism",[51] see reference [52] for an example). Oxygen incorporation plays also a crucial role for mixed conducting SOFC cathodes (see references [53,54] and references therein). Thus, a detailed understanding of oxygen incorporation kinetics is not only a fundamental challenge, but also a challenge of high technological relevance.

When in the following section we consider oxygen incorporation into oxides, it is particularly helpful to bear in mind the example of a bulk conductivity sensor. In such a device, the oxygen partial pressure is translated into an equilibrium value of oxygen content, which itself determines the electronic conductivity. The kinetics of the incorporation process is then equivalent to the sensor's response kinetics; indeed, a simple means to follow the kinetics is the electronic conductance (see, for example, reference [55]). Observation of the conductance is of course an integral technique and usually does not provide spatial resolution (for an example of microelectrode measurements, see Section 6). Typically, space-resolving techniques (e.g. secondary-ion mass spectroscopy, see, for example, reference [56]) analyze frozen-in profiles and are not in situ techniques. In Stuttgart, we developed an optical method that allows us to follow in situ the oxygen incorporation kinetics into strontium titanate as a function of space and time, and much of the progress to be reported is due to this development.[22,37]

The detailed reaction steps can be roughly classified as 1) surface reaction including chemical kinetics at the surface and transport through the subsurface layer, 2) bulk transport, 3) transport across (or along) internal boundaries (the transport along grain boundaries has not yet proven to be important for $SrTiO_3$; nevertheless, we give general information in particular in terms of treating polycrystalline matter). This classification also determines the structure of this Review. For all aforementioned cases, we give: 1) experimental results, 2) theoretical considerations, 3) modeling results in terms of defect chemistry, 4) mechanistic interpretation.

The family of perovskite oxides comprises large-bandgap semiconductors such as $SrTiO_3$ as well as small-bandgap materials or even metallic conductors such as $SrFeO_3$. Moreover, a complete solid solution series $Sr(Fe_xTi_{1-x})O_{3-\delta}$ exists[40] in which (almost) all members exhibit the undistorted cubic perovskite structure. Thus, the effects of cation composition as well as of oxygen nonstoichiometry on the materials properties can be investigated without interference from crystallographic aspects. Increasing substitution of Ti (empty d orbitals) by Fe (partially occupied d orbitals) gives rise to drastic changes in the electronic structure of the materials and also affects the various transport properties to a different degree (see Section 7 for more details).

Before we start with the detailed considerations let us also emphasize the practical significance of our model material $SrTiO_3$. Since large and appropriately doped single crystals are readily available, it is an often used substrate material, for example, for the deposition of superconducting oxide films. The use of $SrTiO_3$ bicrystalline substrates (and of even more complex structures) induces formation of respective grain boundaries with interesting properties also in the deposited superconductor films.[57] With a sufficiently high electron concentration (induced by doping or treatment in strongly reducing atmosphere) it even becomes superconducting itself, albeit at temperatures as low as 0.4 K.[58] Although $SrTiO_3$ does not transform into a ferroelectric phase upon cooling because of quantum fluctuations,[59] its high dielectric permittivity at room temperature (ca. 300) is exploited in several electroceramic functions.[60] Strontium titanate based materials are discussed as alternative high-permittivity dielectric in field-effect transistors and DRAM memory devices.[61] Since the dielectric properties of the solid solution materials $(Ba_xSr_{1-x})TiO_3$ can be tuned by applied DC voltages,[62] they are used in microwave devices and switchable optical waveguides. For these applications, insight into long-time ageing processes under applied electrical bias and thus a detailed understanding of their defect chemistry is important. Owing

Rotraut Merkle studied chemistry in Stuttgart. After a Diploma thesis in Theoretical Chemistry she received her PhD in Physical Chemistry. In 1998 she joined the department of Physical Chemistry at the Max-Planck-Institute for Solid State Research in Stuttgart. Her research interests range from fundamental aspects of point defect formation and transport in ionic solids to detailed investigations of reaction kinetics at oxide surfaces (preferentially applying in situ methods), and also to solid-oxide fuel cells, gas sensors, and heterogeneous catalysis.

Joachim Maier studied chemistry at the University of Saarbrücken, received his PhD there in 1982, and completed his habilitation at the University of Tübingen in 1988. He has lectured at Tübingen, at MIT as a foreign faculty member, at the University of Graz as a visiting professor, and at the University of Stuttgart as an honorary professor. As director of the physical chemistry department (since 1991) of the Max-Planck-Institute for Solid State Research his main interest lies in the conceptual understanding of chemical and electrochemical phenomena involving solids as well as in their use in materials science.

to its high refractive index of 2.4, $SrTiO_3$ can even serve as a gem stone. It can act as a host material for phosphors such as Pr^{3+}; in this context control of morphology and defect concentrations is crucial for a good quantum efficiency.[63] Besides TiO_2, $SrTiO_3$ is one of the most studied photocatalytic materials.[64,65] The water splitting efficiency can be increased, for example, by appropriate doping, to optimize the magnitude and position of the band gap.[66]

At elevated temperatures $SrTiO_3$ can be used as a key material for resistive oxygen sensors.[47] In particular, materials in the $SrTiO_3$-$SrFeO_{3-\delta}$ solid solution series are suitable for sensing oxygen or combustible gases, depending on the actual operation mode.[48] In its donor-doped form, exhibiting a high electronic conductivity in a reducing gas atmosphere, strontium titanate is applied as an anode in ceramic fuel cells (see for example reference [67]). The advantage of such perovskites over Ni-YSZ composite anodes becomes obvious when methane (or other hydrocarbons) is used as fuel because coke deposition on the electrode can be minimized.[68] In all of these last examples, the kinetics of the oxygen surface reaction plays a decisive role in device performance.

When we extend our focus to perovskite analogues containing transition metals with a partially filled d shell, rather complex crystallographic, electronic, and magnetic structures can develop,[69] resulting in a huge number of applications: high-temperature superconductors, ferromagnetic materials, magnetoresistive materials, materials for SOFC electrodes (and electrolytes, for empty d orbitals), ferroelectrics (and piezoelectric or pyroelectric materials) for sensors, actuators, or memory devices etc. The list can easily be prolonged such that—even though oxygen incorporation into $SrTiO_3$ is used herein only as a model—even the detailed discussion of this specific material alone is of enormous relevance.

2. Defect Chemistry in Ionic Solids Exemplified for Fe-Doped $SrTiO_3$

Before discussing the kinetic issues of oxygen exchange, let us clarify the relevant equilibrium properties of our model material. The point defects are of double importance: 1) they are the decisive species enabling mass transport, and 2) they are very reactive acid–base and redox-active centers. Therefore, the knowledge of the ionic and electronic point defect concentrations and their mobilities is an essential prerequisite for the further understanding of the kinetic behavior of a material. From thermodynamic considerations it follows that at nonzero temperatures any given material—owing to the configuration entropy—must contain a finite concentration of point defects (zero-dimensional defects, see for example references [70,71] for a more detailed treatment). In the simplest case we may consider a binary oxide MO in which we can neglect point defects in the metal-ion sublattice. Then we are concerned with oxygen vacancies $V_O^{\bullet\bullet}$, oxygen interstitials O_i'', and also electronic point defects (e', $h^\bullet$) (for definition of the Kröger–Vink defect nomenclature,[72] see Table 1). Together, these defects allow for finite compositional variations $MO_{1-\delta}$ corresponding to valence changes given in Equation (1).

$$\Delta\delta/2\,O_2 + MO_{1-\delta} \rightleftharpoons MO_{1-\delta+\Delta\delta} \qquad (1)$$

In this way the oxide responds to a change in oxygen partial pressure. Figure 1 shows the drastic changes in the internal redox chemistry (e' correspond to Ti^{3+} (more exactly $e' = Ti^{3+} - Ti^{4+}$), $h^\bullet$ correspond to O^- (more exactly $h^\bullet = O^- - O^{2-}$)), and acid–base chemistry ($V_O^{\bullet\bullet}$, O_i'') when traversing the phase width. On the level of Equation (1), cationic

Table 1: Defect equilibria [Eqs. (2)–(7)] for Fe-doped $SrTiO_{3-\delta}$.

	Reaction[a]		Mass-action law
oxygen incorporation:	$1/2\,O_2 + V_O^{\bullet\bullet} \rightleftharpoons O_O^x + 2\,h^\bullet$	(2)	$K_{ox} = \frac{[h^\bullet]^2}{\sqrt{pO_2}[V_O^{\bullet\bullet}]}$
$Fe^{3+/4+}$ redox reaction:	$Fe_{Ti}^x \rightleftharpoons Fe_{Ti}' + h^\bullet$	(3)	$K_{Fe} = \frac{[Fe_{Ti}'][h^\bullet]}{[Fe_{Ti}^x]}$
band-gap excitation:	$0 \rightleftharpoons e' + h^\bullet$	(4)	$K_{bg} = [e'][h^\bullet]$
	Conservation conditions:		
iron mass balance:	$[Fe]_{tot} = [Fe_{Ti}'] + [Fe_{Ti}^x]$	(5)	
charge neutrality:	$2[V_O^{\bullet\bullet}] + [h^\bullet] = [Fe_{Ti}'] + [e']$	(6)	
	$2[V_O^{\bullet\bullet}] \approx [Fe_{Ti}']$	(7)	

[a] Kröger–Vink nomenclature:[72] $V_O^{\bullet\bullet}$: main character: chemical species, V = vacancy; subscript: site (for example, O = regular oxygen site); superscript: charge relative to perfect lattice; $^\bullet$, $'$, x correspond to singly positive, singly negative, and neutral effective charge.

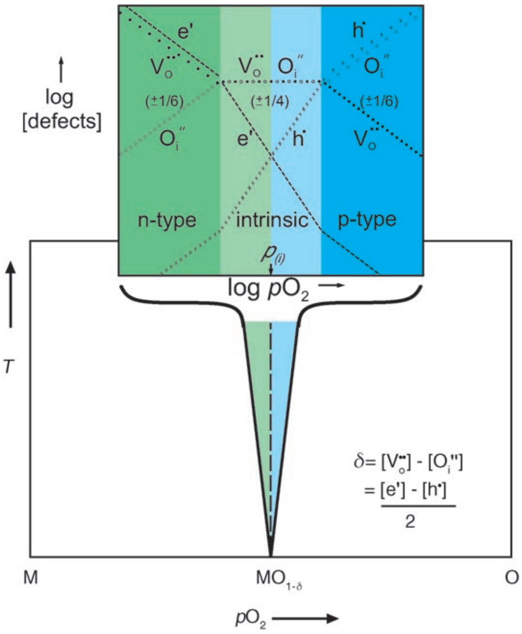

Figure 1. Phase diagram of an oxide MO depending on temperature T and oxygen partial pressure pO_2. Within the extension of the phase width, drastic changes in the defect concentrations occur which can be described by the defect-chemical model (note the logarithmic scale). Reproduced from reference [71] with permission from Wiley.

defects do not introduce a new compositional parameter. The situation is different in a ternary compound such as $SrTiO_3$, in which additional compositional complications come from deviations in the Sr/Ti ratio corresponding to metal ion defects. Fortunately, in the window of interest (i.e. at temperatures typically up to 900 °C), $SrTiO_3$ behaves as a pseudobinary; that is, possible nonstoichiometric Sr/Ti ratios are frozen, or put differently: metal vacancies are immobile and act as native dopants (see reference [73] for the connection of full point defect equilibration with constrained equilibria). To outweigh the significance of native or unknown foreign dopants, it is advisable to dope $SrTiO_3$ deliberately.[74] This is one reason why we deal with iron-doped $SrTiO_3$; another one is the occurrence of valence changes, which adds another redox reaction to the set of defect-chemical reactions. It is this valence change that allows us to follow the local oxygen content by optical spectroscopy (see below).[35]

In $SrTiO_3$, iron is substituted by titanium and exhibits a mixture of the oxidation states of +III and +IV (Fe^{4+}, rather unusual in aqueous chemistry, is stabilized in this case by occupying a site tailored for the Ti^{4+} cation in the host crystal lattice; this substitutional defect is denoted Fe_{Ti}^{x}). Charge compensation for the Fe^{3+} ions (i.e. Fe_{Ti}') occurs only to a small extent by electron holes $h^{\bullet}$ in the valence band, but predominantly by the formation of oxygen vacancies $V_O^{\bullet\bullet}$. A significant oxygen deficiency can also be generated in undoped $SrTiO_3$ under strongly reducing conditions such as 20 % H_2 at 1200 °C.[75] In this case, the oxygen vacancies are compensated by excess electrons (Ti^{3+}), which give rise to the black color of the reduced material. Fe^{3+} is an "acceptor dopant", as it leads to an increase of all defects with a positive charge relative to the perfect lattice, including electron holes. As the term "acceptor dopant" refers to the electronic case, but ionic defect concentration changes are also caused, we prefer the term "negative dopant". The relative fractions of Fe^{3+} and Fe^{4+} depend on the external control parameters temperature T, oxygen partial pressure pO_2, and total iron concentration $[Fe]_{tot}$. The defect reactions are summarized in Table 1 (square brackets denote concentrations, constant terms are included in the mass-action constants).

In the dilute regime, the defect concentrations can be calculated from mass-action laws (for a detailed treatment see, for example, references [70,71,76,77]). Figure 2 shows the variation of the Fe^{4+} and Fe^{3+} concentrations: the lower the temperature and the higher the value of pO_2, the higher is the proportion of Fe^{4+}. Figure 3a gives an overview of the dependence of all point defects on pO_2 and demonstrates that in this large-bandgap material the electronic defects are clearly in minority. The mass-action constants were determined from a combination of experiments (see reference [78], also incorporating data from earlier investigations[38,39,79–82]). The concentration of oxygen vacancies for given external control parameters can be measured by thermogravimetry if the total iron concentration $[Fe]_{tot}$, and therefore $[V_O^{\bullet\bullet}]$, is sufficiently high. For slightly doped single crystals, $[Fe_{Ti}^{x}]$ can alternatively be determined from its characteristic optical absorption at 590 nm[35] (corresponding to the brown color of oxidized samples; stoichiometric $SrTiO_3$ is colorless, and Fe_{Ti}' does not absorb in the visible range) and related to $[V_O^{\bullet\bullet}]$ by Equation (7) (Table 1). The electronic charge carrier concentrations can be obtained from the conductivity under conditions of predominant electronic conduction (if their mobilities are known, for example, from Hall measurements[82]). Figure 3b shows a typical set of conductivity data, revealing n- and p-type electronically conducting regimes in which roughly $\sigma \propto (pO_2)^{\pm 1/4}$ power

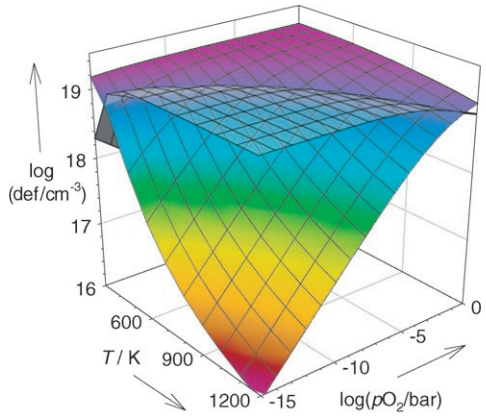

Figure 2. Equilibrium Fe^{4+} (color) and Fe^{3+} (transparent gray) concentrations in 0.1 mol % Fe-doped $SrTiO_3$ as a function of T and pO_2 calculated from the defect chemical model.[78]

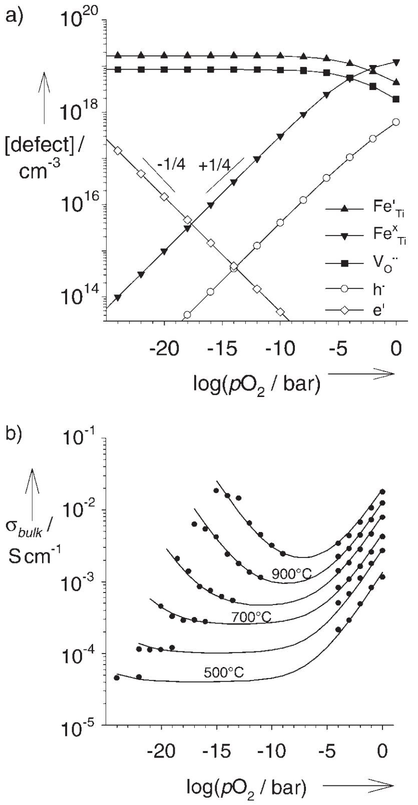

Figure 3. a) Point defect concentrations in Fe-doped (0.1 mol %) $SrTiO_3$ (700 °C) calculated from the defect-chemical model.[78] b) Bulk conductivity of a polycrystalline Fe-doped (0.1 mol %) $SrTiO_3$ sample. In the pO_2-independent region, the conductivity is predominantly ionic (oxygen vacancies), whereas at very low and high pO_2 n- and p-type electronic conductivity prevails.

laws are valid, as well as a pO_2-independent regime at lower temperatures, indicating ionic conductivity. In the perovskite structure, the mobile ionic charge carriers are the oxygen vacancies $V_O^{\bullet\bullet}$. Their mobility can be obtained from the ionic conductivity (if $[V_O^{\bullet\bullet}]$ is fixed, for example, by negative doping), or, less directly, from the chemical diffusion coefficient of oxygen (see Section 3).

Further complications in the defect chemical model arise from the interaction between ionic point defects. The electrostatic attraction of Fe_{Ti}' and $V_O^{\bullet\bullet}$ primarily leads to the formation of Fe_{Ti}'-$V_O^{\bullet\bullet}$ pairs (an oxygen vacancy in the first coordination shell around Fe_{Ti}').[83] An EPR investigation at elevated temperatures showed that these defect pairs are completely dissociated above 300 °C.[84] This study also demonstrated that defect interactions become perceptible (in the form of non-unity activity coefficients), even at dopant concentrations below 0.1 at. %.

Since the structural distortions at the crystal's surface and at grain boundaries change the standard chemical potentials, all defect concentrations there are expected to differ from the bulk values. A more detailed discussion of this aspect is given in reference [85] and Sections 4 and 6. As already mentioned, at temperatures below 1200 °C we can consider the Sr/Ti ratio as frozen. At very high temperatures this constraint is removed and the partial Schottky reaction will lead to the formation of strontium vacancies.[86] In contrast, when the temperature is lowered towards room temperature the oxygen content freezes. Section 9 deals with such cases as far as experiment and theory is concerned. In summary, $SrTiO_{3-\delta}$ is one of the few examples for which the defect chemistry is understood in great detail, a fact that is an important prerequisite and basis for the possibility of a detailed kinetic analysis. Owing to complications by extremely long equilibration times and formation of secondary phases for donor-doped $SrTiO_3$,[87–89] we will concentrate in this article on the acceptor-doped materials.

3. Reaction and Transport: General Considerations

As we do not face formation, motion, or annihilation of interfaces during oxygen incorporation reactions, the only processes under consideration are reactions at the surface, particle transfer from the surface into the crystal, and particle transport within the crystal including transport across or along internal interfaces. Mechanistically these processes are distinguished by whether or not particles change their identity, change their environment in structural terms, or perceive different electrical potentials.

For a more detailed discussion it suffices to consider the general case of a heterogeneous reaction in which particles change nature and environment (for more details see also references [71,90,91]). As extensions to complicated situations are straightforward, and as in fact many chemical reactions turn out to be pseudo-monomolecular, it is instructive to consider the reaction given in Equation (8), in which A is converted into B while the location is simultaneously changed from x to $x' = x + \Delta x$.

$$\mathrm{A}(x) \rightleftharpoons \mathrm{B}(x') \tag{8}$$

The driving force (reaction affinity $\mathscr{A}$) is given by the difference in the electrochemical potential ($\tilde{\mu}$), which is composed of the chemical potential (expressed as $\mu^0 + RT\ln c$ for dilute situations, whereby μ^0 is independent of the concentration c) and the electrical potential term $zF\phi$ (z = particle charge, F = Faraday constant). If $x \equiv x'$, or, more realistically, if structural and electrical potential differences between x and x' are negligible, the reaction is homogeneous, whereas for $\mathrm{A} \equiv \mathrm{B}$ a transport process is met. The most simple case is transport within a given phase (i.e. $\mu^0(x) = \mu^0(x')$) if no internal electrical field exists between x and x' (i.e. $\phi(x) = \phi(x')$). This case refers to bulk transport. If the latter condition is not fulfilled, we refer to transport within space–charge regions.

Applying simple chemical kinetics to Equation (8) gives the reaction rate in Equations (9) and (10).

$$\Re = \tilde{\vec{k}}[\mathrm{A}(x)] - \tilde{\overleftarrow{k}}[\mathrm{B}(x')] \tag{9}$$

$$= \tilde{\vec{k}}[\mathrm{A}(x)]\left(1 - e^{-\mathscr{A}/RT}\right) = -\tilde{\overleftarrow{k}}[\mathrm{B}(x')]\left(1 - e^{+\mathscr{A}/RT}\right) \tag{10}$$

In these equations, $\mathscr{A} = -\Delta\tilde{G} = -[\tilde{\mu}(\mathrm{B}(x')) - \tilde{\mu}(\mathrm{A}(x))]$. The quantities $\vec{k}$ and $\overleftarrow{k}$ denote the forward and backward rate constants, and the tilde designates that electrical potential changes ($\Delta\phi$) are included according to Equations (11) and (12) (α = symmetry factor,[92] $0 \leq \alpha \leq 1$).

$$\tilde{\vec{k}} = k_0 \exp(-\Delta\vec{G}/RT)\exp(-\alpha z F\Delta\phi/RT) \tag{11}$$

$$\tilde{\overleftarrow{k}} = k_0 \exp(-\Delta\overleftarrow{G}/RT)\exp((1-\alpha) z F\Delta\phi/RT) \tag{12}$$

For a homogeneous chemical reaction, the driving force as well as the activation energy is purely chemical ($-\mathscr{A} = \Delta G = \Delta\vec{G} - \Delta\overleftarrow{G}$). For bulk transport, forward and backward activation free energies are the same, that is, $\tilde{\vec{k}} = \tilde{\overleftarrow{k}} = k$, and Equation (9) directly leads to Equation (13) (we restrict ourselves to the quasi-one-dimensional case).

$$\Re = -k\Delta c = -(k\Delta x)\nabla c \tag{13}$$

This expression corresponds to Fick's first law $j = -D\nabla c$ as long as the jump distance Δx is so small relative to the thickness that the difference can be replaced by the differential, which is a good approximation for macroscopic samples. In the case of chemical diffusion to be considered later, local electrical field effects do not disappear, but couple two counter fluxes such that Equation (13) is again valid for the electroneutral oxygen transport.

In contrast, homogeneous and heterogeneous reactions are generally characterized by nonlinear force–flux relations [see Eq. (10)]. If $\mathscr{A} \ll RT$, linearization is possible, leading to Equation (14), whereby the prefactor is the exchange rate

$\Re_0 = \vec{k}\left[\widehat{\mathrm{A}}\right] = \overleftarrow{k}\left[\widehat{\mathrm{B}}\right] = \sqrt{\vec{k}[\widehat{\mathrm{A}}]\overleftarrow{k}[\widehat{\mathrm{B}}]}$ (the arc denotes equilibrium concentrations).

$$\Re = \Re_0 \mathscr{A} \tag{14}$$

Unlike for transport, this condition is very harsh as A contains the difference in the standard chemical potentials $\mu_\mathrm{B}^0 - \mu_\mathrm{A}^0$, which is usually a significant value. Equation (14) holds only in an extremely narrow range, but it is a good approximation if one starts out from equilibrium and perturbs it slightly (relaxation kinetics). A more convenient way to express linear rate-driving force relations is to use the concentration perturbation $\delta c = c - \widehat{c}$ as driving force [Eq. (15)].

$$\Re = \Re_0 \frac{\partial \mathscr{A}}{\partial c} \partial c = \bar{k}_\mathrm{R}^\delta \delta c \tag{15}$$

The effective (phenomenological) rate constant $\bar{k}_\mathrm{R}^\delta$[93] then involves the exchange rate $\Re_0$ and the derivative $\partial\mathscr{A}/\partial c$ is taken at equilibrium (the superscript δ emphasizes that $\bar{k}_\mathrm{R}^\delta$, as well as D^δ defined in Equation (17), describe the kinetics of stoichiometry change). Equation (15) can also be obtained from the detailed kinetics[13] and is actually of a more extended validity range for (pseudo)monomolecular mechanisms. For dilute situations ($\mu = \mu^0 + RT\ln c$), $\partial\mathscr{A}/\partial c$ is given by inverse concentrations, and the exchange rate $\Re_0$ is a product of rate constants and concentrations. The connection with the rate constants of the elementary steps $\vec{k}$, $\overleftarrow{k}$ will be discussed below. Note again [see Eq. (8)] that these considerations are general and also include the transport case that can be conceived as a hopping or "rearrangement reaction" with zero standard affinity. In this special case, the exchange rate is related to the conductivity, whereas the product of $\Re_0$ and $\partial\mathscr{A}/\partial c$ corresponds to the diffusion coefficient, which is proportional to the mobility.[71] The transport across an internal boundary can be described by an effective rate constant analogous to the surface reaction. Table 2 gives the relations that are valid for small deviations from equilibrium. For all these cases, the flux can be expressed as a product of an inverse chemical resistance and an inverse chemical capacitance. This allows elegant modeling of complex situations in terms of chemical or electrochemical equivalent circuits.[94] Far from equilibrium one has to resort to Equation (9) but can neglect the forward or backward reaction. Both situations will be extensively exploited in the mechanistic evaluation. The insight gained for the kinetics of stoichiometry changes (described in the following sections) is, although not transferable literally, also valuable for the understanding of electrode and isotope exchange kinetics.[13,14]

Table 2: Equations for chemical transport across surface, bulk, and grain boundaries in situations close to equilibrium for dilute charge carriers.

Step:	Transport equation:		Kinetic coefficient:
surface reaction	$j = -\bar{k}^\delta \delta c\|_\mathrm{surface}$	(16)	effective rate constant
chemical diffusion	$j = -D^\delta \nabla c$ (Fick's law)	(17)	chemical diffusion coefficient
grain boundary	$j = -\bar{k}_\mathrm{gb}^\delta \delta c\|_\mathrm{gb}$	(18)	grain boundary rate constant

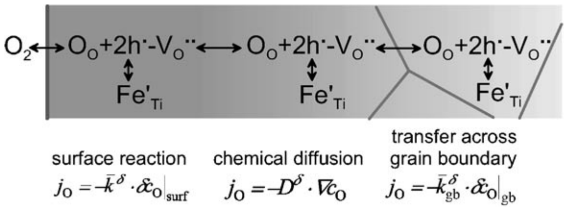

Figure 4. Transport processes involved in the change in oxygen content of a mixed conducting oxide, shown for Fe-doped $SrTiO_3$.

The equilibration of the oxygen nonstoichiometry of the sample with the surrounding pO_2 at elevated temperatures is a multistep process. Figure 4 gives an overview, and further mechanistic details of the individual transport processes are discussed in Section 4–6. At the surface, molecular oxygen is transformed into oxide ions in the first bulk layer in a reaction involving electrons as well as ion transfer steps. The subsequent chemical diffusion of oxygen in the bulk material comprises the movement of ionic and electronic defects (here: oxygen vacancies $V_\mathrm{O}^{\bullet\bullet}$ and electron holes $h^\bullet$) so that in total neutral oxygen is transported through the sample. In many polycrystalline materials, grain boundaries represent an additional barrier for charge and mass transport (examples where this is not the case are mentioned in Section 6 and 7). In the following analysis we will—for simplicity's sake—assume that one of the processes determines the overall rate (although more complicated situations can also be handled). In addition we assume that the oxygen uptake in the surface layer itself is small relative to the bulk and transients in the interfacial composition can be neglected (quasi-stationary conditions). Depending on the actual conditions (material, pO_2, T, total sample dimension and/or grain size, surface coatings), each of the above steps can limit the overall sample relaxation, which leads to characteristic concentrations profiles. Such profiles can be recorded in an elegant way on single-crystal or bicrystal samples by in situ spatially resolved optical spectroscopy.[37]

Characteristic examples are shown in Figure 5. If the surface reaction is slow relative to the chemical bulk diffusion (the borderline is represented by $\bar{k}^\delta l \approx D^\delta$, whereby l is half the crystal thickness), the concentration inside the single crystal is almost homogeneous (Figure 5a). A more detailed analysis is then required to determine what elementary process of the surface reaction scheme is rate-determining. In contrast, pronounced spatial profiles are obtained in the diffusion-limited case (Figure 5b). For the bicrystal shown, it is evident that the grain boundary is a strong barrier for oxygen transport, leading to steplike internal profiles (Figure 5c; movies of these experiments can be accessed on our homepage[95]). Very fast relaxation

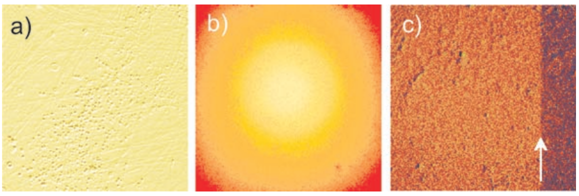

Figure 5. Spatially resolved oxygen concentration after a pO_2 change measured on Fe-doped $SrTiO_3$.[17,18,22,37] $[Fe]_{tot} = 0.3$ mol%, 650 °C, sample dimensions $6\times6\times1$ mm. The two large faces are glass sealed so that oxygen can enter only through the small faces. Bright color indicates a high oxygen vacancy concentration. a) single crystal, surface reaction is limiting; b) single crystal, bulk diffusion is limiting; c) 24° [001] symmetrical tilt bicrystal, blocking grain boundary (arrow indicates position of the grain boundary, oxygen diffuses in from the right-hand side).

processes can be studied by analyzing their response (e.g. conductivity change) upon variable frequency pO_2 oscillations.[47] Although this method allows the distinction between surface-reaction and bulk diffusion limitation, it is restricted to small pO_2 changes and thus yields limited information about the surface reaction mechanism.

4. Surface Reaction

Let us start with the surface reaction and first discuss how the surface rate constant $\bar{k}^{\delta}$ is related to the underlying chemical kinetics in general and to the mechanism of the surface reaction for the case of Fe-doped $SrTiO_3$ in detail. Figure 6 shows the time evolution of the oxygen concentration for the case that the surface reaction is limiting (corresponding to Figure 5a). The concentration profiles are horizontal and the intercepts provide information about the kinetics. Since the concentration is homogeneous within the sample, Equation (16) can easily be integrated to yield for any time a simple exponential decay for the normalized oxygen concentration change [Eq. (19); l = half the sample thickness, one-dimensional case].

$$\frac{\delta c(t)}{\delta c(0)} = \frac{c_O(t)-c_O(\infty)}{c_O(0)-c_O(\infty)} = e^{-\bar{k}^{\delta}t/l} \tag{19}$$

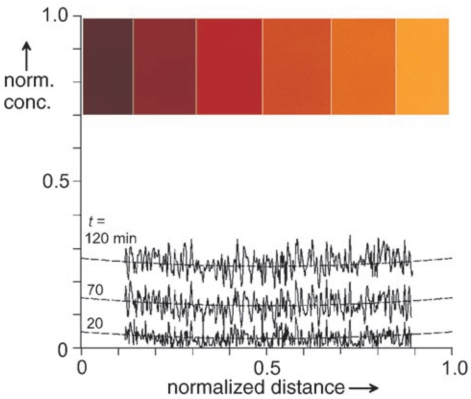

Figure 6. Time evolution of the normalized concentration profiles corresponding to the experiment shown in Figure 5a.[17] Inset: Snapshots of the sample.

Figure 7 compares the measured effective rate constants $\bar{k}^{\delta}$ for bare and coated surfaces of Fe-doped $SrTiO_3$ (note that such an exponential law is always valid for (pseudo)first order reactions, but in general holds only close to equilibrium).

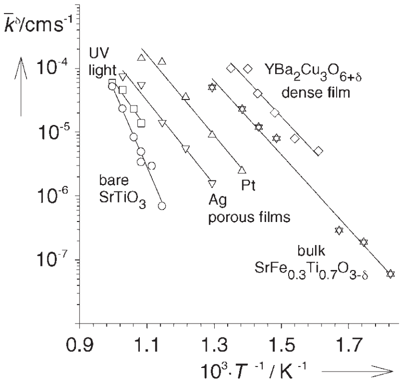

Figure 7. Effective surface rate constants $\bar{k}^{\delta}$ of oxygen incorporation for bare and coated Fe-doped $SrTiO_3$. ○: bare Fe-doped $SrTiO_3$; □: bare Fe-doped $SrTiO_3$ under UV irradiation; ▽ and △: porous Ag and Pt layers; ◇: dense, mixed conducting $YBa_2Cu_3O_{6+\delta}$ layer; ✡: incorporation into bulk $SrFe_{0.3}Ti_{0.7}O_{3-\delta}$. Reproduced from reference [158] with permission from Springer.

For further interpretation, $\bar{k}^{\delta}$ can be traced back to the reaction mechanism of the surface reaction (for more details see references [13,14]). The surface reaction itself is a multistep reaction comprising adsorption, electron transfer, O–O bond dissociation, and incorporation of atomic oxygen species into oxygen vacancies. As mentioned above, for the mechanistic analysis, we assume that one of these steps, the rate-determining step (rds), is specifically much slower[96] than the others, which are in quasi-equilibrium (this implies that the whole reaction affinity drops according to the rds), and that oxygen storage in the surface is negligible. Thus, virtually immediately the reaction rate is uniformly given by the rate of the rds.

For the surface reaction, electrical potential steps $\Delta\phi$ between x and x' must be taken into account. Although the affinity of the rds (being equal to the total reaction affinity, which refers to the incorporation of neutral oxygen into the neutral bulk) does not contain a contribution from $\Delta\phi$, electrical potential drops may influence $\tilde{\bar{k}}$. Guided by our experience from $SrTiO_3$ grain boundaries,[97] we approximate the surface potential drop as being constant in the limited pO_2 and T range covered by kinetic experiments. Thus, in the further treatment, the values $\overrightarrow{k}$ and $\overleftarrow{k}$ include $\exp(-\alpha zF\Delta\hat{\phi}/RT)$ and $\exp((1-\alpha)zF\Delta\hat{\phi}/RT)$ as constant potential contributions, even though we dropped the tilde.

Now let us be as specific as possible and refer to the detailed reaction mechanism to be validated later (see Table 3 for dilute defect concentrations and low adsorbate coverage). Assuming the second ionization reaction [Eq. (25)] is rate-determining, we obtain Equation (20).

$$\Re = \Re_{\mathrm{rds}} = \vec{k}[\mathrm{O_2}^-][\mathrm{e}'] - \overleftarrow{k}[\mathrm{O_2}^{2-}] \tag{20}$$

Close to equilibrium this equation becomes Equation (21).

$$\Re = \Re_0\left(\frac{[\mathrm{O_2^-}]}{[\widehat{\mathrm{O}}_2^-]}\frac{[\mathrm{e}']}{[\widehat{\mathrm{e}}']} - \frac{[\mathrm{O_2^{2-}}]}{[\widehat{\mathrm{O}}_2^{2-}]}\right) = \Re_0\left(\frac{\delta[\mathrm{O_2^-}]}{[\widehat{\mathrm{O}}_2^-]} + \frac{\delta[\mathrm{e}']}{[\widehat{\mathrm{e}}']} - \frac{\delta[\mathrm{O_2^{2-}}]}{[\widehat{\mathrm{O}}_2^{2-}]}\right) \tag{21}$$

In this case, $\Re_0 = \sqrt{\vec{k}\overleftarrow{k}[\widehat{\mathrm{O}}_2^-][\widehat{\mathrm{e}}'][\widehat{\mathrm{O}}_2^{2-}]}$ and δ denotes the deviation from equilibrium. The preceding and succeeding reactions [Eqs. (24), (26), and (27)] are in quasi-equilibrium (K_{pre}, K_{suc}) with the band-gap equilibrium [Eq. (4)] to yield Equation (22).[98]

$$\frac{\delta[\mathrm{O_2^-}]}{[\widehat{\mathrm{O}}_2^-]} = \frac{\delta[\mathrm{e}']}{[\widehat{\mathrm{e}}']} = \frac{-\delta[\mathrm{h}^\bullet]}{[\widehat{\mathrm{h}}^\bullet]} \quad \text{and} \quad \frac{\delta[\mathrm{O_2^{2-}}]}{[\widehat{\mathrm{O}}_2^{2-}]} = -2\frac{\delta[\mathrm{V_O^{\bullet\bullet}}]}{[\widehat{\mathrm{V}}_\mathrm{O}^{\bullet\bullet}]} + 2\frac{\delta[\mathrm{h}^\bullet]}{[\widehat{\mathrm{h}}^\bullet]} \tag{22}$$

Finally, the reaction rate is given by Equation (23).[99]

$$\begin{aligned} \Re &= \Re_0\left(2\frac{\delta[\mathrm{V_O^{\bullet\bullet}}]}{[\widehat{\mathrm{V}}_\mathrm{O}^{\bullet\bullet}]} + 4\frac{\delta[\mathrm{h}^\bullet]}{[\widehat{\mathrm{h}}^\bullet]}\right) \\ &= \Re_0\left(\frac{2}{[\widehat{\mathrm{V}}_\mathrm{O}^{\bullet\bullet}]} + \frac{\delta[\mathrm{h}^\bullet]}{\delta[\mathrm{V_O^{\bullet\bullet}}]}\frac{2}{[\widehat{\mathrm{h}}^\bullet]}\right)\delta[\mathrm{V_O^{\bullet\bullet}}] = -2\frac{\Re_0}{RT}\frac{\partial\mu_\mathrm{O}}{\partial c_\mathrm{O}}\delta c_\mathrm{O} \end{aligned} \tag{23}$$

Table 3: Tracing back reaction rate $\Re$ and effective rate constant $\bar{k}^\delta$ to the surface reaction mechanism.

Most probable surface reaction mechanism for Fe-doped $SrTiO_3$:[12]

$$\mathrm{O_2} \rightleftharpoons \mathrm{O_2}^- + \mathrm{h}^\bullet \qquad \text{fast} \tag{24}$$

$$\mathrm{O_2}^- + \mathrm{e}' \rightleftharpoons \mathrm{O_2}^{2-} \qquad \text{rds}^{[a]} \tag{25}$$

$$\mathrm{O_2}^{2-} \rightleftharpoons 2\mathrm{O}^- \qquad \text{rds}^{[a]} \tag{26}$$

$$\mathrm{O}^- + \mathrm{V_O^{\bullet\bullet}} \rightleftharpoons \mathrm{O_O}^{\mathrm{x}} + \mathrm{h}^\bullet \qquad \text{fast} \tag{27}$$

surface reaction rate:

$$\Re = \vec{k}[\mathrm{O_2^-}][\mathrm{e}'] - \overleftarrow{k}[\mathrm{O_2^{2-}}] = \vec{k}'\frac{K_{\mathrm{pre}}p\mathrm{O_2}}{[\mathrm{h}^\bullet]}[\mathrm{e}'] - \overleftarrow{k}'\frac{[\mathrm{h}^\bullet]^2}{K_{\mathrm{suc}}[\mathrm{V_O^{\bullet\bullet}}]^2} \tag{28}$$

approximation far from equilibrium:

$$\Re \approx \vec{\Re} = \vec{k}'K_{\mathrm{pre}}p\mathrm{O_2}\frac{[\mathrm{e}']}{[\mathrm{h}^\bullet]} \quad \text{or} \quad \Re \approx \overleftarrow{\Re} = \frac{-\overleftarrow{k}'}{K_{\mathrm{suc}}}\frac{[\mathrm{h}^\bullet]^2}{[\mathrm{V_O^{\bullet\bullet}}]^2} \tag{29}$$

approximation close to equilibrium:

$$\frac{1}{2}\Re_{\mathrm{O_2}} \propto -j_\mathrm{O} = \bar{k}^\delta \delta c_\mathrm{O} \tag{30}$$

effective rate constant:

$$\boxed{\bar{k}^\delta = 4\frac{\Re_0}{RT}\frac{\partial\mu_\mathrm{O}}{\partial c_\mathrm{O}} = 4\Re_0\left(\frac{1}{[\mathrm{V_O^{\bullet\bullet}}]} + \chi\frac{4}{[\mathrm{h}^\bullet]}\right)} \tag{31}$$

exchange rate

$$\Re_0 = \sqrt{\vec{k}\overleftarrow{k}[\widehat{\mathrm{O}}_2^-][\widehat{\mathrm{e}}'][\widehat{\mathrm{O}}_2^{2-}]} \tag{32}$$

[a] Rate-determining step.

This result could also be directly derived from Equation (14) but without any information on the range of validity (for more details see references [13,14]). Close to equilibrium, comparison with Equation (14) yields the effective rate constant $\bar{k}^\delta$, as given in Equation (31), Table 3. The proportionality of $\bar{k}^\delta$ to $\Re_0\partial\mu_\mathrm{O}/\partial c_\mathrm{O}$ is general; only the prefactor (here $2/RT$) depends on the molecularity of the assumed reaction. The dependence of $\bar{k}^\delta$ on pO_2 arises from the reaction mechanism ($\Re_0$) as well as from bulk defect chemistry ($\partial\mu_\mathrm{O}/\partial c_\mathrm{O}$). Whereas the first term is proportional to an inverse chemical resistance, the latter term is the inverse of a "chemical capacitance",[94] which describes the material's ability to accommodate changes in oxygen stoichiometry upon a change in pO_2. (Note that the same capacitive term appears in Equation (40) for chemical diffusion. The fact that $\partial\mu_\mathrm{O}/\partial c_\mathrm{O}$ refers to the first bulk layer as δc_O does expresses the fact that storage in the surface layer has been neglected). For dilute conditions, the chemical capacitance can further be expressed by bulk defect concentrations, see Equation (31) and the related term in Equation (23).[99] In the presence of redox-active centers, a "trapping factor" $0 \le \chi \le 1$ is included (through $\delta[\mathrm{h}^\bullet]/\delta[\mathrm{V_O^{\bullet\bullet}}]$), which is discussed in more detail in Section 5.

For a mechanistic understanding of a reaction, one usually determines the reaction orders of all involved reactants and products. In the case of the gas–solid reaction, this is more difficult to achieve than in the case of homogeneous fluid phase reactions in which reactants and products can be added independently to the reaction mixture. For the reaction considered herein, pO_2 is of course an independent variable. In contrast, the point defects in the oxide are linked to each other (and to the external pO_2) by the defect equilibria, and a variation of the Fe dopant content implies the preparation of a new (single-crystal) sample (i.e. is an "ex situ parameter"[100]). Therefore, the possibilities for concentration variation are limited. Since a temperature change affects the potentially involved defect concentrations as well as K_{pre}, K_{suc}, $\vec{k}$, and $\overleftarrow{k}$, only an effective overall activation energy can be obtained. The reaction order of oxygen can be determined from a series of large changes in pO_2 (i.e. the forward reaction rate $\vec{\Re}$ in Equation (29) dominates the overall reaction rate), leading from the same initial pO_2 to various higher pO_2 values. At short times after the pO_2 step, the defect concentrations are still close to their initial values so that the variation of $\vec{\Re}_{\mathrm{ini}}$ with the various final pO_2 values gives the reaction order of oxygen. Such a series is shown in Figure 8. The measured dependence $\vec{\Re}_{\mathrm{ini}} \propto (pO_2)^{0.9\pm0.1}$ indicates an oxygen reaction order close to unity and implies that molecular oxygen species must be involved in the rds (e.g. adsorbed superoxide O_2^- or peroxide O_2^{2-}).[12] The exponents from the other series contain contributions from the involved point defects, as does the overall pO_2 dependence. In the case of Fe-doped $SrTiO_3$, additional mechanistic information can be obtained from the effect of UV irradiation (energy larger than the band gap), which linearly accelerates the incorporation rate but does not affect the rate of removal.[12,101] This behavior indicates that a single conduction electron is involved before or in the rds. The resulting most probable

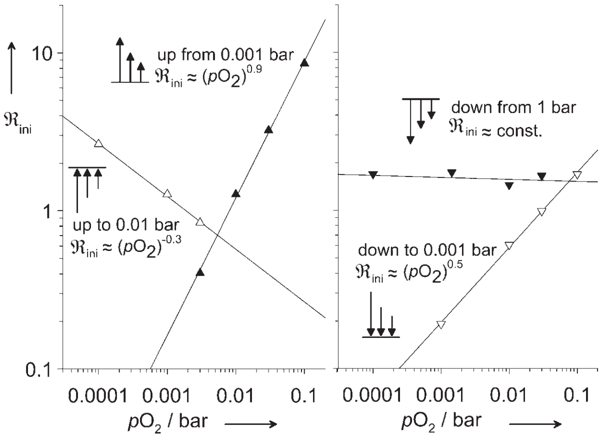

Figure 8. pO_2 dependence of initial reaction rates $\Re_{ini}$ for chemical oxygen incorporation into Fe-doped (0.3 mol%) $SrTiO_3$ single crystals at 730°C. Data compiled from reference [12].

reaction mechanism is given in Table 3. Unfortunately, reactions (25) and (26) representing the rds yield the same kinetic expressions so that these two cases cannot be further distinguished.

A number of coating materials, for example, porous Ag and Pt films, strongly accelerate the oxygen exchange kinetics (see Figure 7)[17] and lower the effective activation energy from about 2.5 eV to 1–1.5 eV. The effects can be rationalized on the basis of the mechanism identified for the bare surface. Platinum and silver are known to dissociate oxygen easily. In the case of a dense mixed conducting $YBa_2Cu_3O_{6+\delta}$ layer, the surface reaction occurs very fast on the $YBa_2Cu_3O_{6+\delta}$ surface,[78] and oxygen is transferred into the $SrTiO_3$ in the form of oxide ions. A porous layer of alkaline earth metal oxides was also found to accelerate oxygen incorporation,[102] which might be related to stabilization of adsorbed superoxide or peroxide ions.

The (100) orientation corresponds to the most stable surface of $SrTiO_3$ as confirmed by experiment and DFT calculations.[103] The (100) face can exhibit SrO or TiO_2 termination, both nonpolar and with comparable surface energy.[103] Both terminations coexist after surface polishing and annealing, but both terminations can also be deliberately obtained in pure form.[104,105] A recent study indicates differences in the photocatalytic behavior at room temperature, whereby the TiO_2 termination is more active because of easier electron transfer to adsorbed oxygen species.[105] Although adsorbed oxygen species (e.g. O^-, O_2^-, O_2^{2-}) have been identified on a number of oxides,[106] it is a demanding task to reveal their concentrations under the relevant conditions ($pO_2 \approx 1$ bar, $T \geq 300$°C) since the usual surface analysis techniques typically require ultrahigh vacuum. To our knowledge, reliable concentrations of adsorbed oxygen species on acceptor-doped large-band-gap oxides have not yet been determined. This topic is further complicated by the fact that the charge of the adsorbates will lead to deviations from Langmuir's isotherm.[107] Nevertheless, the assumption of a low adsorbate coverage is supported by the fact that the chemisorption step requires the transfer of electron(s) to the adsorbates, which is energetically not very favorable for an acceptor-doped large-band-gap oxide, and that the experiments are carried out at high temperatures. A recent review on oxygen adsorbates on SnO_2 concluded that a detectable coverage (but still below 0.1%) with superoxide ions is present only on reduced samples and at temperatures below 150°C.[108] Quantum chemical calculations may help to gather the necessary information.

Because the surface represents a structural distortion, the point defect concentrations at the surface must be different from the bulk values, but are not quantitatively known (since they are in equilibrium with the bulk, we assumed identical pO_2 dependencies for our kinetic analysis). This also means that in general the surface is expected to exhibit an excess charge and a compensating "space charge zone" similar to the situation at grain boundaries (for more details see Section 6). An increase of the iron concentration in a near-surface region of 12 nm thickness (measured by secondary-ion mass spectroscopy SIMS) was interpreted in reference [109] as an indication for a positive surface charge leading to Fe_{Ti}' accumulation. Recent $^{16}O^{18}O$ isotope exchange experiments followed by extensive SIMS analysis with extremely high spatial resolution give direct evidence for a $V_O^{\bullet\bullet}$ depletion space–charge zone extending about 8 nm from the surface into the bulk.[110,111] Since the step in the $^{18}O/(^{16}O+^{18}O)$ concentration ratio resulting from the impeded transport though the surface space charge layer is smaller than the concentration step between gas phase and first crystal layer caused by the surface reaction, we consider the proper surface reaction as the limiting process. (Note that in the case of a perceptible surface depletion, δc_O in Equation (30) has to be referred to a distance from the geometrical surface at which the depletion effects are negligible). Oxygen isotope exchange on $Pb(Zr_{0.35}Ti_{0.65})O_3$ perovskite films also yields evidence for significant $V_O^{\bullet\bullet}$ depletion in a surface space–charge zone.[112]

5. Bulk Diffusion

After oxygen has been incorporated into the first crystal layer by the surface reaction, further transport occurs by chemical diffusion. Figure 9 shows the characteristic concen-

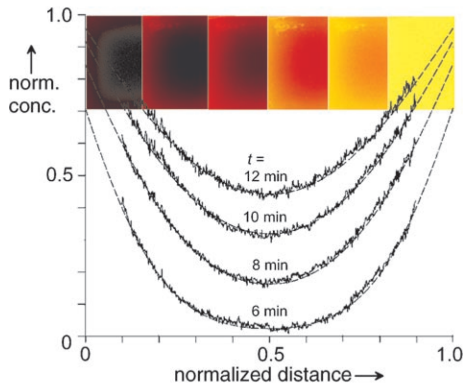

Figure 9. Time evolution of the concentration profiles corresponding to the experiment shown in Figure 5 b.[22,37] Inset: Snapshots of the sample.

tration profiles measured on single crystals for the case that bulk chemical diffusion is limiting (Figure 5b), that is, the surface reaction is relatively fast and/or the sample thickness is large, and the diffusion coefficient D^δ is constant. The oxygen concentration change integrated over the whole sample then follows the relations in Equations (33) and (34) for the limits of short time and $t \rightarrow \infty$, respectively ($L =$ sample thickness, one-dimensional case).

$$\frac{c_O(t)-c_O(0)}{c_O(\infty)-c_O(0)} = \frac{4}{L}\sqrt{\frac{t D^\delta}{\pi}} \tag{33}$$

$$\frac{c_O(t)-c_O(\infty)}{c_O(0)-c_O(\infty)} = \frac{8}{\pi^2}\, e^{-\pi^2 D^\delta t/L^2} \tag{34}$$

As discussed in Section 3, diffusion can be regarded as a "rearrangement" reaction such that the exchange rate in Equation (15) corresponds to the conductivity term and $\Re_0 \partial\mathscr{A}/\partial c$ to the diffusion coefficient. Since the chemical diffusion describes the concentration change of a neutral component, the fluxes of the ionic (here: $V_O^{\bullet\bullet}$) and electronic ($h^\bullet$) charge carriers [Eqs. (35) and (36) in Table 4] are coupled by the electroneutrality condition. Also here we can start out from the kinetic master equations for two carriers, with the local electrical potential then coupling the two rate equations. This enables one to describe chemical diffusion also for nonlinear cases.[91,113] For our purpose it suffices and is more convenient to use the description in terms of linear laws using electrochemical potential gradients as driving forces.[114,115] As a result, the flux of neutral oxygen [Eq. (39)] comprises the ambipolar conductivity $\sigma^\delta = \sigma_{ion}\sigma_{eon}/(\sigma_{ion}+\sigma_{eon})$ (subscript eon indicates "electronic"; i.e. electron or hole conduction) as the transport parameter (corresponding to the exchange rate of the chemical diffusion process) and the gradient in the chemical potential $\partial\mu_O/\partial x$ as the driving force. The ambipolar conductivity is obviously determined by the least conductive ensemble (ionic or electronic), and therein by the fastest particle. Comparison with Equation (17) shows that the bracketed term is the chemical diffusion coefficient D^δ [Eq. (40) in Table 4] containing a term $\partial\mu_O/\partial c_O$ analogous to the surface effective rate constant [cf. Eq. (31)]. If one electronic and one ionic defect sort determines transport, this term is given by these defect concentrations (if dilute) [Eq. (40)].[99] In the presence of internal reactions again trapping factors χ have to be invoked.[21,99] For redox-active ions, an internal reaction of the form of Equation (3) $\mathrm{Fe_{Ti}^x} \rightleftharpoons \mathrm{Fe_{Ti}'} + h^\bullet$ leads to trapping of highly mobile "free" holes $h^\bullet$ at "immobile" $\mathrm{Fe_{Ti}^x}$ centers (for Fe-doped $SrTiO_3$, the holes need an activation energy of around 1 eV to escape from this potential well). Qualitatively, this means that as the "chemical capacitance" $\propto (\partial\mu_O/\partial c_O)^{-1}$ in Equation (40) increases, the sample can accommodate larger oxygen nonstoichiometry changes upon a given pO_2 change because not only "free" holes are formed, but also "trapped holes" in the form of $\mathrm{Fe_{Ti}^x}$. Thus, D^δ has to decrease as long as the other terms in Equation (40) remain unchanged. The actual value of χ depends on the mass-action constant of the respective trapping reaction, a detailed quantitative treatment can be found in references [21,71]. If defect interactions lead to the formation of mobile defect pairs (e.g. different valence states), the expression for σ^δ also changes.[21]

Table 4: Chemical bulk diffusion exemplified for oxygen in oxides.

chemical diffusion in the bulk:

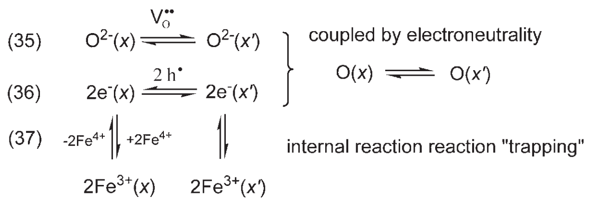

$$(35)\quad O^{2-}(x) \xrightleftharpoons{V_O^{\bullet\bullet}} O^{2-}(x')$$

$$(36)\quad 2e^-(x) \xrightleftharpoons{2\,h^\bullet} 2e^-(x')$$

coupled by electroneutrality

$$O(x) \rightleftharpoons O(x')$$

$$(37)\quad 2Fe^{3+}(x) \xrightleftharpoons[+2Fe^{4+}]{-2Fe^{4+}} \qquad 2Fe^{3+}(x') \rightleftharpoons$$

internal reaction reaction "trapping"

coupled charge carrier fluxes:

$$j_{O^{2-}} = -1/2\, j_{e^-} = j_O \tag{38}$$

$$j_{O^{2-}} = -\frac{\sigma_{ion}}{4F^2}\nabla\tilde{\mu}_{O^{2-}} = -\frac{\sigma_{ion}}{4F^2}(\nabla\mu_{O^{2-}} - 2F\nabla\phi)$$

$$j_{e^-} = -\frac{\sigma_{eon}}{F^2}\nabla\tilde{\mu}_{e^-} = -\frac{\sigma_{eon}}{F^2}(\nabla\mu_{e^-} - F\nabla\phi)$$

$$j_O = -\frac{1}{4F^2}\sigma^\delta\nabla\mu_O = -\left(\frac{1}{4F^2}\sigma^\delta\frac{\partial\mu_O}{\partial c_O}\right)\nabla c_O \tag{39}$$

chemical diffusion coefficient:

$$\boxed{D^\delta = \frac{\sigma^\delta}{4F^2}\frac{\partial\mu_O}{\partial c_O} = \frac{RT\sigma^\delta}{4F^2}\left(\frac{1}{[V_O^{\bullet\bullet}]} + \chi\frac{4}{[h^\bullet]}\right)} \tag{40}$$

with $0 \le \chi \le 1$ "trapping factor"

and $$\sigma^\delta = \frac{\sigma_{ion}\sigma_{eon}}{\sigma_{ion}+\sigma_{eon}} \tag{41}$$

$$D_{ion} \le D^\delta \le D_{eon} \quad \text{for } \chi = 1 \tag{42}$$

D^δ can be further traced back to defect diffusion coefficients D_{ion}, D_{eon} (in addition to defect concentrations) both being proportional to the defect mobilities[116] as indicated in Equation (42). D^δ varies between the (usually smaller) diffusion coefficient of the ionic defect D_{ion} and the typically larger D_{eon}. For strong trapping, D^δ can even drop below the value of D_{ion}. The trapping reaction is most effective when both oxidation states of the ion are present in comparable amounts. For Fe-doped $SrTiO_3$ under typical experimental conditions, the trapping effect leads to $D^\delta \approx 3 D_{V_O^{\bullet\bullet}}$, that is, D^δ differs only slightly from the vacancy diffusion coefficient.[22] The experimental data recorded over an extended temperature range in Figure 10 illustrate the

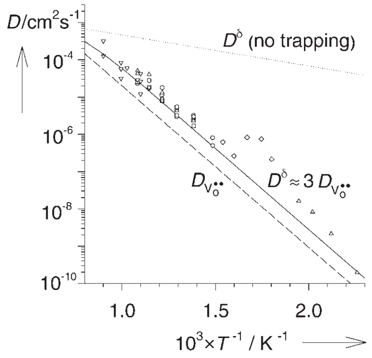

Figure 10. Chemical diffusion coefficient D^δ for Fe-doped $SrTiO_3$ samples with $[Fe]_{tot} \approx 0.3$ mol%. Symbols: experimental data; lines: calculated from the defect model. The dashed line shows the (concentration-independent) vacancy diffusion coefficient $D_{V_O^{\bullet\bullet}}$; the dotted line shows the calculated D^δ values in the absence of "hole trapping" at $\mathrm{Fe_{Ti}^x}$ centers. Reproduced from reference [22] with permission from Elsevier.

validity of this approximation. In this regime, D^{δ} is independent of pO_2 and the total iron concentration (which is not the case in general). The activation energy of $D_{V_O^{\bullet\bullet}}$ amounts to 0.9 eV, a value typical for many oxides with the perovskite structure.[117,118] Figure 10 also shows that neglecting the trapping leads to predicted D^{δ} values that are orders of magnitude too high, especially at lower temperatures. Since typical impurities in oxides such as iron and manganese are redox-active, at least in a certain pO_2 and T range, and are present even in nominally pure single crystals, the trapping effect on D^{δ} can in general not be neglected, even if these impurities do not result in conductivity changes.[119]

In the above considerations we neglected the pO_2 dependence of D^{δ}. Very recently, D^{δ} in 1.8 mol% Al-doped $SrTiO_3$ was measured directly over an extended pO_2 range of 1–10^{-20} bar and found to vary by about two orders of magnitude, the maximum occurring around 10^{-8} bar.[120] Again the dependence can be described in detail in terms of the underlying defect chemistry; again trapping effects (here the pure Coulombic effect between Al_{Ti}' and $h^{\bullet}$ (i.e. O^-)) prove important.

As a result of varying D^{δ} values, the concentration profiles can deviate from their typical smooth shape. Such an experiment is shown in Figure 11 for a Fe-doped $SrTiO_3$ single crystal.[121] Under strongly reducing conditions (hydrogen treatment), the sample is predominantly ionically conducting and trapping effects are not very strong, so D^{δ} approaches D_{eon}. Under oxidizing conditions with strong trapping by iron centers, $D^{\delta} \approx 3D_{V_O^{\bullet\bullet}}$ holds as derived above, thus the diffusion coefficient is orders of magnitude smaller. When the atmosphere is changed from oxygen to hydrogen, the high D^{δ} value in the outer, already reduced part of the sample gives rise to a flat section in the concentration profile followed by a steep decrease at the transition to the low-D^{δ} region. Under such conditions one can describe the process by the motion of a diffusion front. Very large deviations from equilibrium also occur in high DC voltage experiments with nonreversible electrodes.[29,30] Although more involved, the defect chemical analysis gives a quantitative description.[30]

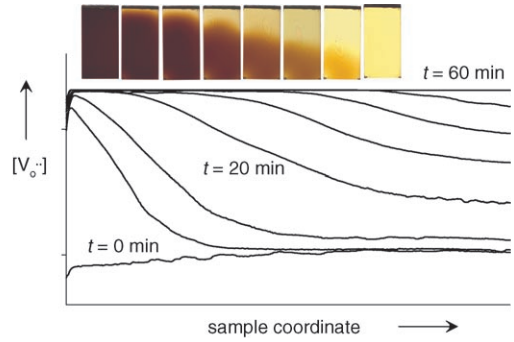

Figure 11. Vacancy concentration profiles in Fe-doped (0.2 mol%) $SrTiO_3$ after pO_2 change from 1 bar to ca. 10^{-30} bar at 530°C. Inset: true-color photographs of samples quenched at different time after the pO_2 change; oxygen enters the sample from top.

6. Grain Boundaries

In polycrystalline samples, transport across as well as along grain boundaries can be accelerated or impeded relative to the bulk properties.[122] We will first focus on the case of impeded transport across grain boundaries (gb), which is observed for many acceptor-doped large-band-gap oxides. To show the transport across a single, well defined grain boundary, Figure 12 gives an example for oxygen diffusion into a Fe-doped $SrTiO_3$ bicrystal containing a symmetrical tilt grain boundary.[18] Oxygen enters the sample from the right-hand side and travels fast up to the grain boundary. Then the grain boundary dramatically impedes further transport, leading to a pronounced step in the concentration profiles. The oxygen flux across a blocking grain boundary can be described by an effective rate constant $\bar{k}^{\delta}_{gb}$ [see Eq. (18)].

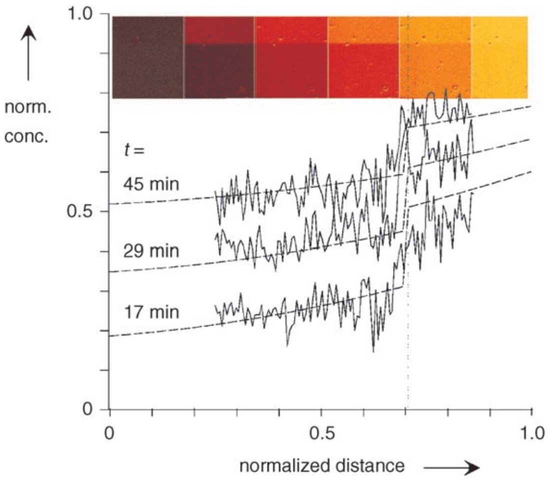

Figure 12. Time evolution of the concentration profiles corresponding to the experiment shown in Figure 5 c;[18] oxygen enters the sample from the right-hand side. Inset: Snapshots of the sample (oxygen enters from the top).

A high-resolution transmission electron microscopy image of a 5.4° [001] symmetrical tilt grain boundary is shown in Figure 13 a[126] (the impedance spectrum in Figure 15 demonstrates that this grain boundary also exhibits a blocking character). The image shows that this grain boundary is free of secondary or amorphous phases, and that it is atomically sharp. The structural mismatch is "condensed" into a regular array of edge dislocations (bright areas in Figure 13 a) with an almost undisturbed lattice structure in between. Thus, structural effects can be ruled out as the decisive reason for the strong blocking of mass as well as charge transport. This interpretation is also in agreement with the effective capacitance derived from impedance spectroscopy which suggests that the blocking region is several tens of nanometers thick, which is much larger than the core thickness of the grain boundary. The overall behavior can be consistently explained by the space–charge model depicted in Figure 14. The core of the grain boundary, that is, the region of about 1 nm width where the structural distortion is concentrated into the array of edge dislocations, represents a structurally modified region

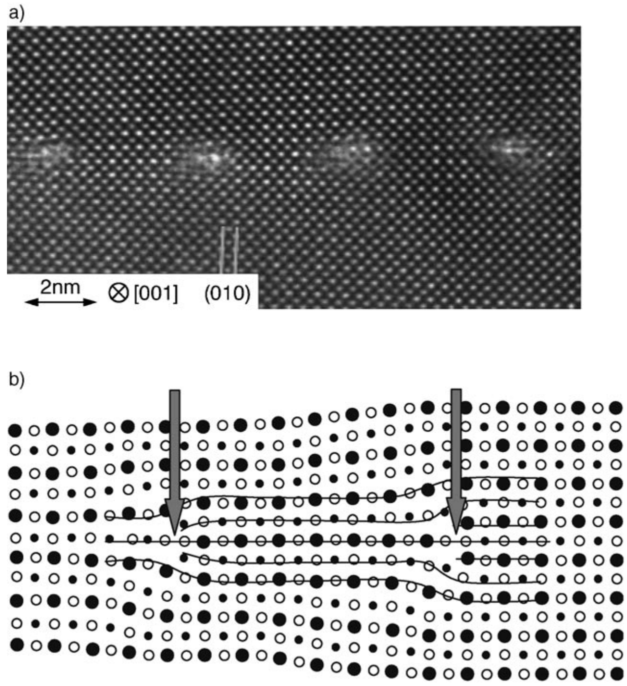

Figure 13. a) HRTEM image of an Fe-doped (0.05 mol%) $SrTiO_3$ bicrystal with 5.4° [001] symmetrical tilt grain boundary (reproduced from reference [126] with permission from the American Ceramic Society). The bright areas are the cores of edge dislocations arranged in an array. b) Corresponding structural model; arrows mark dislocation cores with partially occupied oxygen columns. ⬤: Sr; ●: Ti; ○: O (reproduced from reference [137] with permission from Elsevier).

and therefore the standard chemical potential of all defects differs from their respective bulk values. This leads in general to a charging of the core of the grain boundary, and in the case of Fe-doped $SrTiO_3$, results in a positive charge. Since the crystal as a whole is electroneutral, this excess charge must be compensated in the volume adjacent to the grain boundary. In the case of Fe-doped $SrTiO_3$, the ionic as well as the electronic majority charge carriers are positively charged ($V_O^{\bullet\bullet}$ and $h^{\bullet}$, see Figure 3; the Fe_{Ti}' are immobile under the experimental conditions). Thus, the charge compensation must occur by a depletion of these species in the space–charge zone, and as a consequence $V_O^{\bullet\bullet}$ and $h^{\bullet}$ transport across this type of grain boundary is strongly impeded (Figure 14). Owing to their low concentration, the accumulated e' cannot contribute significantly to the compensation. (For cases in which the space–charge potential leads to an inversion layer, see references [123–125]). As both carriers are needed for the chemical diffusion, there will be a significant chemical resistance exerted by such internal boundaries.

The electronic depletion can be directly detected by impedance spectroscopy in the form of a pronounced grain boundary response (Figure 15).[126,127] The severe depletion of oxygen vacancies was established by DC experiments using electrodes that block the electronic current.[128] The space–charge potential $\Delta\phi = \phi(x=0) - \phi(\text{bulk})$ is determined by the condition that the electrochemical potentials $\tilde{\mu}_i = \mu_i + z_i F\phi$ of the mobile defects of species i are equal in the grain boundary core and in the adjacent crystal region located at $x=0$. The constancy of $\tilde{\mu}_i$ in the space–charge zone then couples the local defect concentrations to the electrical potential [Eq. (43)].

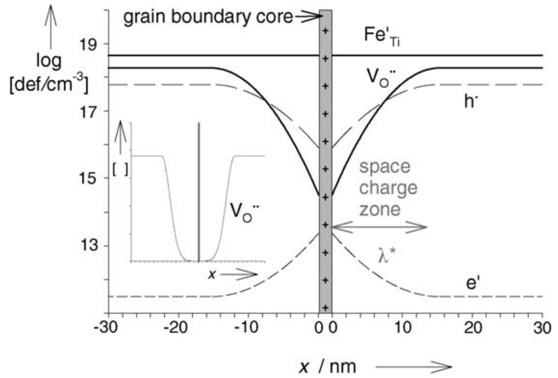

Figure 14. Charge-carrier concentration profiles at a blocking grain boundary in Fe-doped $SrTiO_3$ ($[Fe]_{tot} = 0.1$ mol%, 700°C, $pO_2 = 1$ bar, $\Delta\phi = 0.4$ V). The excess positive charge in the grain boundary core is compensated by adjacent space–charge zones with $V_O^{\bullet\bullet}$ and $h^{\bullet}$ depletion. Note the logarithmic concentration scaling in the main plot and linear scaling in the inset.

$$c_i(x) = c_i(\infty) e^{-z_i F(\phi(x) - \phi(\text{bulk}))/RT} \tag{43}$$

Poisson's equation $\nabla^2\phi = -(F\Sigma z_i c_i)/\varepsilon_0\varepsilon_r$ relates $\phi(x)$ to the charge density, and the combination with Equation (43) yields the concentration profiles. As pointed out earlier, we can to good a approximation assume that the approximately 1-nm-thin grain boundary core does not impede mass or charge transport significantly. As long as the grain boundary core charge does not perceptibly change upon pO_2 change and is thus stationary,[97] the expression $j_{O^{2-}} = -1/2 j_{e^-} = j_O$ still holds (otherwise charging would occur), but within the space–charge zone the partial conductivities σ_{ion} and σ_{eon} and thus σ^{δ} are now position-dependent. Since the differential "slices" of the space–charge zone act as serially connected resistors, one has to integrate over the reciprocal ambipolar conductivity

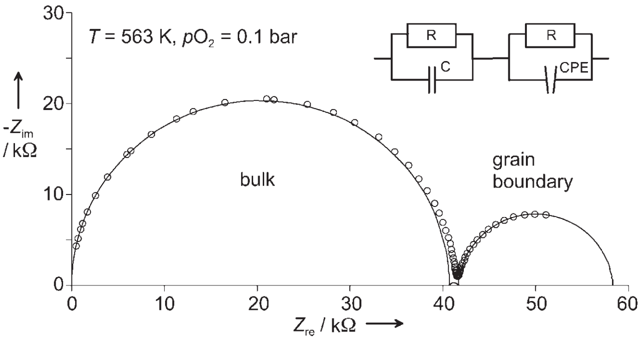

Figure 15. Impedance spectrum of the Fe-doped $SrTiO_3$ bicrystal with a tilt angle of 5.4° (reproduced from reference [126] with permission from the American Ceramic Society). In the corresponding equivalent circuit, the blocking grain boundary is represented by additional resistor and constant phase elements (the further R and CPE elements corresponding to the tiny electrode semicircle are omitted).

Table 5: Transport across blocking grain boundaries and relations for the "Mott–Schottky" depletion case (see for example references [71,133] for more details).

Coefficient for chemical oxygen transport across blocking grain boundaries:

$$\boxed{\bar{k}^{\delta}_{\mathrm{gb}} = \frac{1}{4F^2}\frac{\partial \mu_{\mathrm{O}}}{\partial c_{\mathrm{O}}}\left(\int_{\mathrm{gb}}\frac{1}{\sigma^{\delta}(x)}\mathrm{d}x\right)^{-1} \quad \text{with} \quad \sigma^{\delta} = \frac{\sigma_{\mathrm{ion}}\sigma_{\mathrm{con}}}{\sigma_{\mathrm{ion}}+\sigma_{\mathrm{eon}}}} \qquad (44)$$

"Mott–Schottky" depletion case:

extension of depletion zone[a]	$\lambda^* = \sqrt{\frac{2\varepsilon_0\varepsilon_r}{z_{\mathrm{d}}Fc_{\mathrm{d}}}\Delta\phi}$ (45) with $\Delta\phi = \phi(x=0)-\phi(\mathrm{bulk})$	
chemical transport coefficient	$\bar{k}^{\delta}_{\mathrm{gb}} = \frac{\sigma_{\mathrm{ion}}}{4F^2\lambda^*}\frac{\partial\mu}{\partial c}\left(\frac{e^{2F\Delta\phi/RT}}{2F\Delta\phi/RT}\right)^{-1}$	(46)
electrical resistivity ratio (hole conduction)	$\frac{\rho_{\mathrm{gb}}}{\rho_{\mathrm{bulk}}} = \frac{e^{F\Delta\phi/RT}}{2F\Delta\phi/RT} = \frac{\omega_{\mathrm{bulk}}}{\omega_{\mathrm{gb}}}$	(47)

[a] c_{d} = constant concentration of immobile dopant with charge z_{d} (here: $\mathrm{Fe}_{\mathrm{Ti}}'$ with $z_{\mathrm{d}} = 1$).

$1/\sigma^{\delta}(x)$ to obtain the transport coefficient for oxygen [Eq. (44) in Table 5].[18,129,130] The transport across a blocking grain boundary contains elements analogous to bulk transport [see Eq. (40): the ambipolar conductivity constitutes the relevant "exchange rate"—but is now position dependent] as well as to the surface reaction (on the phenomenological level all processes occurring in the space–charge layer are summed up in the grain boundary transport coefficient $\bar{k}^{\delta}_{\mathrm{gb}}$, and the chemical potential drops in a stepwise manner over this zone [cf. Eqs. (16) and (18)]).

The situation met in Fe-doped $\mathrm{SrTiO_3}$, namely a depletion layer in which an immobile dopant ($\mathrm{Fe}_{\mathrm{Ti}}'$) is the main constituent of the charge density,[131,132] is called the "Mott–Schottky" case.[133] The effective thickness λ^* of the space–charge zone with almost complete $\mathrm{V}_{\mathrm{O}}^{\bullet\bullet}$ and $\mathrm{h}^{\bullet}$ depletion increases with decreasing dopant concentration c_{d} (for given $\Delta\phi$ or given core charge $Q = \lambda^* z_{\mathrm{d}} F c_{\mathrm{d}}$). A typical value is $\lambda^* =$ 25 nm for 0.1 mol% Fe-doped $\mathrm{SrTiO_3}$ ($\Delta\phi = 0.6$ V, $\varepsilon_{\mathrm{r}} = 160$ at 300 °C). The ratio of grain boundary versus bulk resistivity [Eq. (47) in Table 5] for electrical transport across the grain boundary is obtained by integration of $1/[\mathrm{h}^{\bullet}(x)]$ over the whole space–charge zone[134] assuming a constant mobility ($\Delta\phi$ is obtained most reliably from the ratio $\omega_{\mathrm{gb}}/\omega_{\mathrm{bulk}}$ of the semicircle peak frequencies[135]). Owing to the particle charge z_{i} in the exponent, the doubly charged $\mathrm{V}_{\mathrm{O}}^{\bullet\bullet}$ [relevant for chemical transport; Eq. (46)] are much more depleted than the holes $\mathrm{h}^{\bullet}$, which is indeed in agreement with the above-mentioned electrical experiment. Equation (47) also shows that the grain boundary resistance exhibits a larger activation energy than the bulk, the difference being approximately $z_i F\Delta\phi$ (assuming a negligible temperature dependence of the space–charge potential).

If the charge carrier that contributes most to the charge density is mobile, the "Gouy–Chapman" case applies. An accumulation of this defect allows compensation of the core charge within a less extended space–charge region characterized by the Debye length $\lambda = \sqrt{\varepsilon_0\varepsilon_{\mathrm{r}}RT/(2\,z_{\mathrm{d}}^2F^2c_{\mathrm{d}})}$. Detailed expressions for this case can be found in references [71,136].

In general, the magnitude or even the sign of the core charge (and hence of the compensating space charge) cannot be predicted a priori since the standard chemical potentials of the point defects in the grain boundary core are unknown. By deliberately varying the misorientation, the model system of Fe-doped $\mathrm{SrTiO_3}$ bicrystals allows one to obtain some insight into the origin of the core charge. The structural model of such a grain boundary (Figure 13 b) developed on the basis of HRTEM images exhibits two possible atomic arrangements inside the dislocation cores.[137] Nevertheless, in both situations, two oxygen columns approach very closely so that the observation of an increased Ti/O ratio in these regions most likely indicates the formation of oxygen vacancies, thereby relieving some stress in these columns. The amount of positive charge stored in the grain boundary core can be determined from an analysis of the impedance spectra; its variation with tilt angle of the grain boundary is shown in Figure 16. For tilt angles up to 7.8°, these data are consistent with a linear increase expected for a model in which the charge per dislocation core is constant:[137] it is slightly below one elementary charge per perovskite unit cell, corresponding to one singly charged $\mathrm{V}_{\mathrm{O}}^{\bullet\bullet}$ (i.e. an e′ trapped in a $\mathrm{V}_{\mathrm{O}}^{\bullet\bullet}$) per unit cell or a doubly charged $\mathrm{V}_{\mathrm{O}}^{\bullet\bullet}$ in every second unit cell along the dislocation core. It must be emphasized that this correlation between grain boundary geometry and space charge has been proven only for symmetrical low-angle tilt grain boundaries; for general grain boundaries, the situation may well be more complex. In addition to the "intrinsic" cause of the space charge discussed above, one also has to take into account the possibility of

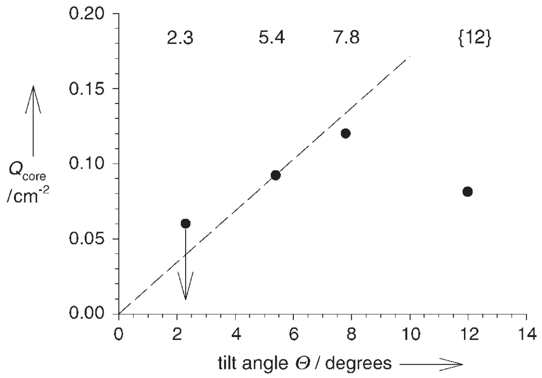

Figure 16. Variation of the core charge with tilt angle for symmetrical low-angle tilt grain boundaries and an asymmetrical 12° grain boundary (in braces). For the 2.3° grain boundary, only an upper limit of Q_{core} could be determined from the impedance spectra. Reproduced from reference [137] with permission from Elsevier.

impurity segregation to the core, which may also lead to a positive space charge potential if segregated cations are accommodated additionally instead of substitutionally. The more open the structure in the grain boundary, the more important this aspect becomes.

In polycrystalline samples, a variety of differently oriented grain boundaries are encountered, ranging from special boundaries such as $\Sigma 3$ grain boundary with small structural distortion[138] to random grain boundaries and grain boundaries that contain amorphous films. On coarse-grained Fe-doped $SrTiO_3$ ceramics (without amorphous grain boundary phases) electrical transport across individual grain boundaries could be studied by impedance spectroscopy by using an array of microcontacts depicted in Figure 17.[139] The peak frequencies ω_{gb} and thus the space charge potentials were found to be rather narrowly distributed around 0.6 V[134] and in accord with the macroscopic value derived from a "brick layer" model assuming cubic grains with identical grain boundary properties (nevertheless some particularly blocking grain boundaries could be disguised by a "current detour" through neighboring grains). Blocking grain boundaries are of course disadvantageous for the utilization as a conductivity sensor. Furthermore, the fact that $V_O^{\bullet\bullet}$ will be more strongly depleted than $h^\bullet$ in such blocking grain boundaries leads to a selective blocking of the ionic transport and to a detrimental polarization in, for example, capacitive devices.[30] However, blocking space charge zones do not only have a "negative" influence, they can also be a prerequisite of functional ceramics such as varistors[140] (i.e. resistors that become conductive above a certain threshold voltage) or "PTCR" devices[141] (resistance increasing with temperature) allowing, for example, for automatic overheating control.

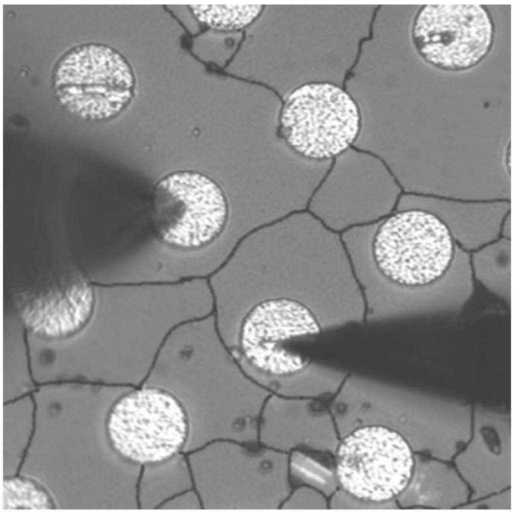

Figure 17. Gold microelectrodes (20 μm diameter) on Fe-doped (0.2 mol %) $SrTiO_3$ ceramic contacted with Pt tips to measure individual grain boundary resistances. Reproduced from refernce [139] with permission from the American Ceramic Society.

From a fundamental viewpoint, an interesting case appears when the grain size approaches λ^*. Then "true size effects" are expected to appear since the depletion layers overlap, that is, they determine the whole properties of the ceramics, and no spot—not even in the middle of the grains—remains charge neutral.[142] This has recently been verified experimentally for nanocrystalline $SrTiO_3$ ceramics.[143]

Let us briefly mention the case of accelerated transport along grain boundaries, although this has not yet been observed for acceptor-doped $SrTiO_3$. Typical situations for polycrystalline materials with enhanced or impeded grain boundary transport are compiled in Figure 18. If mass transport is accelerated along grain boundaries, the time dependence of the concentration change is modified in a characteristic way. Even though there is substantial literature on this topic (see for example reference [144]), the influence of grain boundary confinement or space–charge channeling has been tackled only recently.[145] Spatial profiles for nanocrystalline ceramics can be obtained by numerical simulations as shown in Figure 19. When the characteristic diffusion length $l_{gb} \approx \sqrt{D_{gb}^{\delta} t}$ for grain boundary diffusion is larger that the grain size, the concentration change propagates deep into the sample along the boundaries. Donor-doped titanates are an example in which the bulk chemical diffusion of oxygen is extremely slow because it requires transport of cation vacancies with low mobility[146–149] (oxygen interstitials are impossible in the perovskite lattice). Compared with this process, oxygen diffusion along the grain boundaries is fast, leading to concentration profiles as schematically shown in Figure 18c.

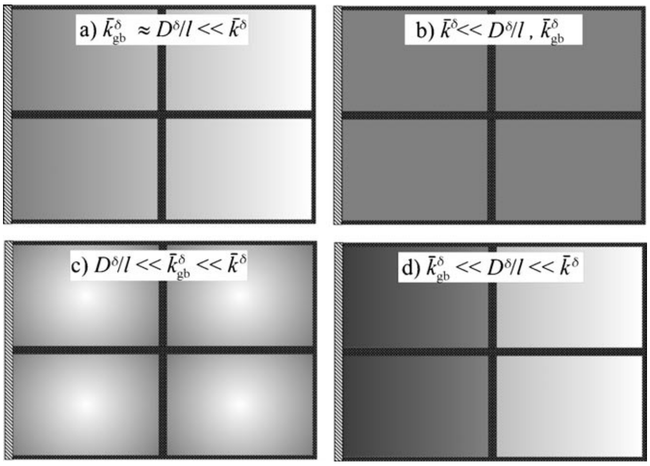

Figure 18. Scheme of oxygen incorporation into a polycrystalline sample of grain size l (color refers to oxygen concentration). Possible situations with respect to the relative magnitude of the bulk diffusion coefficient D^{δ} and the surface ($\bar{k}^{\delta}$) and grain boundary ($\bar{k}_{gb}$, for simplicity assumed to be isotropic) rate constants are shown: a) surface reaction fast, grain boundary neither blocking nor acting as a fast diffusion path; b) surface reaction slow, diffusion inside fast; c) surface reaction fast, grain boundary provides fast diffusion path; d) surface reaction fast, grain boundary blocking. Reproduced from reference [122] with permission from Elsevier.

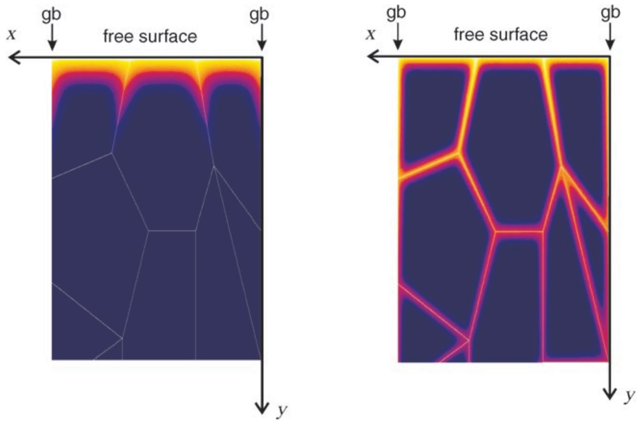

Figure 19. Calculated oxygen concentration profiles for diffusion in nanocrystalline ceramics[176] with enhanced diffusion along grain boundaries when the grain boundary diffusion length is a) smaller that the grain size; b) larger than the grain size.

7. High Iron Content

As already mentioned, the iron content in $Sr(Fe_xTi_{1-x})O_{3-\delta}$ can be continuously increased until the end member of the solid solution series, $SrFeO_{3-\delta}$, is reached. Samples within this series can be divided into two groups of materials:

1. Materials in which the iron concentration is so low that the Fe centers do not interact electronically and represent localized acceptor levels located in the band gap of $SrTiO_3$ ("electron-poor" materials); these are the materials discussed up to here. The absence of electronic interaction effects (Fe 3d band formation, see below) does not imply a complete absence of defect interactions: Reference [84] quantifies how the electrostatic interaction between charged defects affects the Fe_{Ti}'–$V_O^{\bullet\bullet}$ pair formation.
2. Materials in which the iron concentration is high enough so that a partially occupied Fe 3d band forms, which drastically lowers the effective band gap.[40,150] The increasing band width that shows up in the valence-band XPS spectra[150] leads to a significant increase in the electronic mobility, some details of which are still under discussion (polaron[151] or true band conduction[150]). Since electrons in these materials are readily available to be transferred, for example, to adsorbed oxygen species, we denote them as "electron-rich" materials, even though they are still p-type conductors.

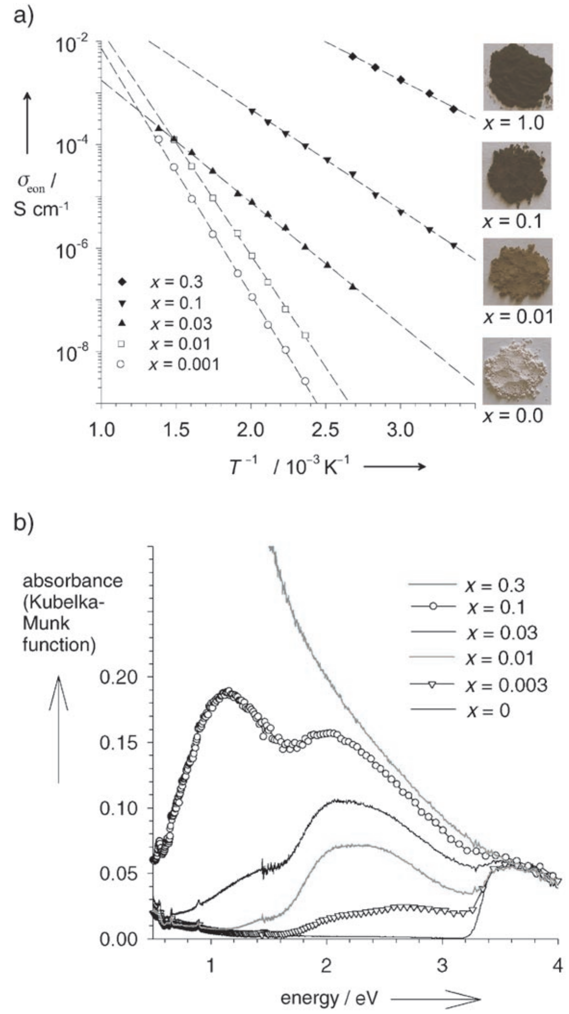

Figure 20. a) Bulk electronic conductivity measured on fully oxidized $SrFe_xTi_{1-x}O_3$ samples with frozen-in oxygen content. The photographs illustrate the color change upon increasing iron content. b) UV/Vis spectra of fully oxidized $SrFe_xTi_{1-x}O_3$ samples (diluted with Al_2O_3 powder), recorded in diffuse-reflection mode.

Figure 20a shows that the electronic conductivity of fully oxidized samples (measured at sufficiently low temperature so that δ does not vary) changes its behavior for $x \geq 0.03$: the absolute values increase drastically while the activation energy drops. This behavior indicates a change in the conduction mechanism resulting from the different electronic structure. The electronic interaction of the iron centers for $x \geq 0.03$ is reflected by the presence of a new low-energy absorption band in the UV/Vis spectra (Figure 20b) as well as in deviations of the magnetic susceptibility from the Curie law;[152] it is also in good agreement with quantum chemical calculations.[153] Typically, in this nondilute regime, the defect chemical reactions can no longer be described by ideal mass-action laws. As a result of the modified temperature dependences of hole concentration and hole mobility, the electronic conductivity of $SrFe_{0.35}Ti_{0.65}O_{3-\delta}$ (in equilibrium with the surrounding pO_2) becomes temperature-independent and is solely determined by pO_2, which is promising for gas-sensor applications.[154] In this respect, it is also beneficial that the grain boundaries lose their blocking character for $x \geq 0.07$.[155,156]

For samples with high dopant and thus high defect concentrations, the approximation $\partial\mu_i/\partial c_i = RT/c_i$ can no longer be applied in Equation (40). For a predominantly electronically conductive material, this term can still be obtained from measured vacancy concentration data according to Equation (48).

$$D^{\delta} = -\frac{D_{V_O^{\bullet\bullet}}}{2}\frac{\partial \ln pO_2}{\partial \ln [V_O^{\bullet\bullet}]} \tag{48}$$

In many mixed-conducting perovskites, the $V_O^{\bullet\bullet}$ concentration shows only a minor pO_2 dependence; accordingly, D^δ is found to be almost pO_2-independent as well (at least for moderate to high values of pO_2; for example, in $Sr(Fe_xTi_{1-x})O_{3-\delta}$[156] or $La_{0.4}Sr_{0.6}FeO_{3-\delta}$[157]).

The different character of the electronic structure of the "electron-rich" $Sr(Fe_xTi_{1-x})O_{3-\delta}$ materials drastically affects oxygen incorporation kinetics.[156,158] The absolute value of $\bar{k}^\delta$ increases by more than two orders of magnitude and the activation energy drops to less than half (see Figure 7). Simultaneously, the reaction mechanism changes so that for these samples only atomic oxygen species, for example, O^-_{ad}, appear in the rds. Thus, as soon as electrons become readily available for transfer to adsorbed oxygen species (which also facilitates the O−O bond dissociation), the first steps in the reaction sequence (24)–(26) are accelerated such that the last step (27), involving ionic motion, becomes the bottleneck. A comprehensive and detailed discussion of oxygen incorporation into "electron-rich" perovskites in general is beyond the scope of this review. These materials were intensively studied in recent years with respect to chemical, electrochemical, and isotope exchange, as well as concerning common mechanistic aspects (see, for example, references [10,15,16,53,54,56,159–165]).

Mixed-conducting perovskites can be applied as catalysts for a number of reactions.[49,50] As an example, Figure 21 shows the catalytic activity of $Sr(Fe_xTi_{1-x})O_{3-\delta}$ for methane oxidation. In the iron concentration range around $x \approx 0.03$, at which the kinetics of the oxygen surface reaction was found to change, the catalytic activity is also modified.[166] Interestingly, not only do the absolute reaction rates increase by more than an order of magnitude, but the CH_4 reaction order[167] and the activation energy also change.

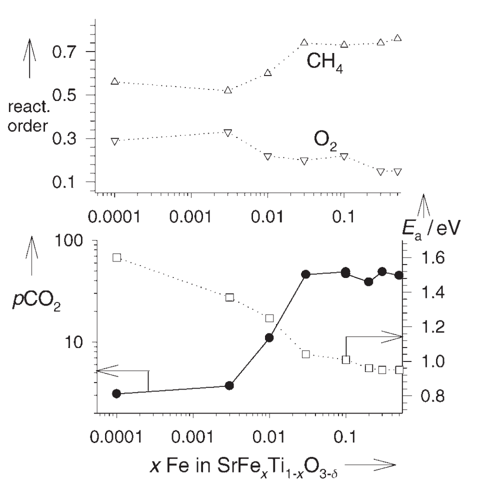

Figure 21. Catalytic oxidation of 1% CH_4 + 3% O_2 over $SrFe_xTi_{1-x}O_{3-\delta}$ at 600°C. ●: resulting CO_2 concentration (normalized to catalyst area); △ and ▽: reaction orders of CH_4 and O_2; □: activation energy E_a.

8. Water Incorporation

Acceptor-doped $SrTiO_3$ can incorporate water on oxygen vacancies[168] leading to the formation of mobile protonic defects [Eq. (49)].[169]

$$H_2O + V_O^{\bullet\bullet} + O_O^x \rightleftharpoons 2OH_O^\bullet \qquad (49)$$

Sc-doped (5 mol%) $SrTiO_3$ exhibits moderate proton conductivity.[170] Water can also be incorporated into the $V_O^{\bullet\bullet}$ in Fe-doped $SrTiO_3$.[171] Here, in contrast to Sc-doped $SrTiO_3$ (in which chemical diffusion occurs through ambipolar motion of $V_O^{\bullet\bullet}$ and $OH_O^\bullet$ with isomorphic diffusion coefficient; just $h^\bullet$ has to be replaced by $OH_O^\bullet$), the availability of iron as redox-active centers implies the presence of three mobile charge carriers (excess protons, oxygen vacancies, and electron holes (free and trapped)) in perceptible amounts, and the kinetics of water uptake becomes rather complex.[172] Since the water uptake changes the vacancy concentration, $[Fe_{Ti}^x]$ and $[h^\bullet]$ also change and can be monitored by optical absorption and conductivity. Figure 22 shows that after an increase in water partial pressure, the conductivity decreases quickly to values lower than expected for the final state and recovers much more slowly. The same overshooting phenomenon is observed for $[Fe_{Ti}^x]$ in spatial resolution by optical spectroscopy. The fast process is a counterdiffusion of protons formed from H_2O at the porous Pt electrodes (in), and electron holes (out), which also decreases $[Fe_{Ti}^x]$. As a result of this hydrogenation, the sample is more reduced than expected for the final state and no longer in equilibrium with

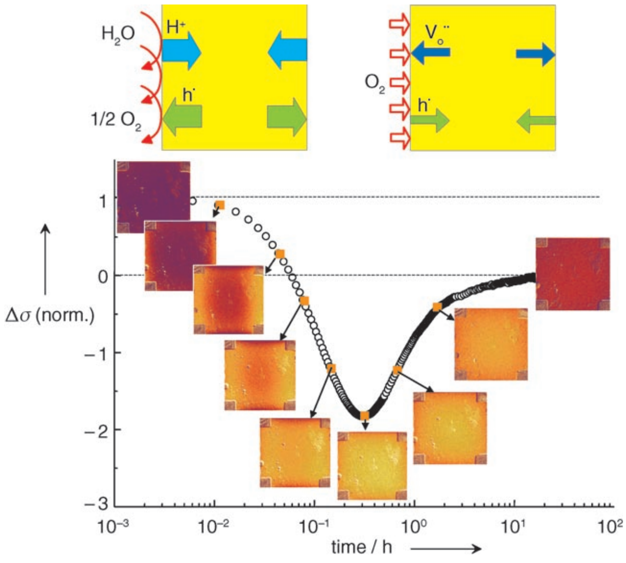

Figure 22. Water incorporation into an Fe-doped (0.05 mol%) $SrTiO_3$ single crystal, pH_2O change from 4 to 20 mbar, pO_2 = 1 bar, 650°C. Insets: Snapshots of the sample in false-color representation showing the local concentrations of Fe_{Ti}^x (incorporation occurs mainly through the vertical edges covered with a porous Pt layer). Note the logarithmic time scale. The cartoons illustrate the fast and the slow part of the overall water incorporation process. Figure adapted from reference [172].

the surrounding pO_2. The oxygenation through counterdiffusion of O^{2-} (through $V_O^{\bullet\bullet}$) and electrons (through $h^\bullet$) occurs more sluggishly than the overshooting. In essence, the acid–base reaction is kinetically decomposed into two redox reactions. This peculiar non-monotonic behavior is enabled by the presence of three mobile charge carriers and the absence of local chemical equilibrium, thus it is a consequence of the complexity of the system and not of the magnitude of the driving force.

9. (Partially) Frozen Defect Chemical Equilibria

Finally, let us briefly discuss situations in which some of the defect chemical reactions are frozen in non-equilibrium conditions. Such cases are important for a number of electrochemical devices such as the "Taguchi-type" gas sensors, varistors, and superconducting materials. When the temperature is lowered, processes involving long-range ionic motion or chemical (surface) reactions typically fail to reach equilibrium. Thus, one can deliberately "freeze in" a certain overall oxygen nonstoichiometry or even a certain $[V_O^{\bullet\bullet}]$ profile. In contrast, internal defect chemical reactions such as the band-gap excitation or trapping reactions are still comparably fast. These scenarios are discussed in detail in references [73,80,100] for differently doped oxides and illustrated in Figure 23 for Fe-doped $SrTiO_3$.[78] Below the freezing temperature, $[V_O^{\bullet\bullet}]$ is constant but $[h^\bullet]$ still varies because of the internal redox reaction [Eq. (3)]. The ionic transference number is markedly different for the equilibrated situation relative to the frozen-in case, in which it increases strongly for low temperatures. Reactions involving only short-range ionic motion (distances of a few unit cells) such as the formation of Fe_{Ti}'–$V_O^{\bullet\bullet}$ defect pairs in $SrTiO_3$ may still equilibrate at room temperature.[84]

In the case of "Taguchi-type" sensors for redox-active gases (for more details see for example reference [173]), which typically operate around 300 °C, the non-equilibrium between the more reduced grain interior and the surrounding pO_2 is essential for its performance. Nevertheless, this situation can give rise to detrimental drift effects (see for example references [174,175]) because on long time scales, small changes in oxygen content are still possible.[176]

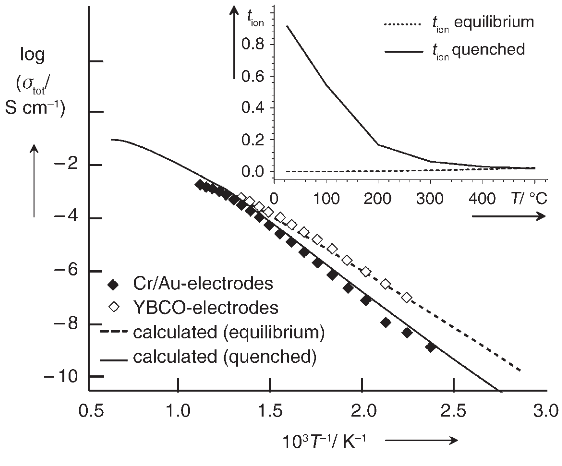

Figure 23. Total conductivity of Fe-doped (0.25 mol%) $SrTiO_3$ at $pO_2 = 1$ bar. Symbols: experimental data; ◇: equilibrium enabled by catalytically active $YBa_2Cu_3O_{6+\delta}$ electrodes; ◆: $[V_O^{\bullet\bullet}]$ frozen in at ca. 500 °C (less active Cr/Au electrodes); lines: calculated data. Inset: Calculated ionic transference number $t_{ion} = \sigma_{ion}/\sigma_{tot}$ for equilibrium and frozen-in case. Data compiled from reference [78].

10. Summary and Outlook

In this overview we have shown that, although it is a complex multistep process, equilibration of an oxide with the surrounding oxygen partial pressure can be investigated and understood in great detail on the macroscopic, phenomenological level as well as in terms of microscopic (atomistic) aspects. One necessary requirement is the detailed understanding of the defect chemistry. Such a comprehensive understanding is not only worthwhile from a fundamental standpoint, it is also of significant technological relevance: Each of the involved processes of surface reaction, bulk diffusion, and transport across grain boundaries is of importance for the functioning of electrochemical devices, which can, in turn, then be optimized by using this knowledge. For the example of a conductivity sensor, crucial properties such as its response time can be purposefully modified over orders of magnitude by varying temperature, doping content, surface structure, or microstructure. Although phenomenological kinetics is able to give an overall description of changes in oxygen stoichiometry, microscopic investigations identifying, for example, the exact nature and concentration of reactive surface species would lend valuable support to the suggested reaction mechanisms. Because of the difficulties of surface-sensitive in situ experiments, atomistic simulations through quantum chemical calculations are expected to develop into a complementary tool of significant importance for the exploration of reaction mechanisms (see, for example, references [177–179]).

We thank former and current members of the department for valuable discussions, particularly Palani Balaya, Roger De Souza, Jürgen Fleig, Janez Jamnik, and Jong-Sook Lee. We thank also Gabriel Harley (University of California) for proofreading the manuscript. Technical support from the service groups, workshops, and many other members of the two Max Planck Institutes in Stuttgart is gratefully acknowledged.

Received: March 6, 2007

[1] G. Tammann, *Lehrbuch der Metallkunde*, Voss, Leipzig, **1932**.
[2] W. Jost, *Diffusion und chemische Reaktion in festen Stoffen*, Steinkopff, Dresden, **1937**.
[3] C. Wagner, *Z. Phys. Chem. Abt. B* **1933**, *21*, 25–41.
[4] C. Wagner, *Prog. Solid State Chem.* **1975**, *10*, 3–16.
[5] H. Schmalzried, *Solid State Reactions*, VCH, Weinheim, **1981**.
[6] K. Hauffe, *Reaktionen in und an festen Stoffen*, Springer, Berlin, **1966**.

[7] A. T. Fromhold, *Theory of Metal Oxidation*, North-Holland, Amsterdam, **1980**.

[8] M. Rohnke, J. Janek, J. A. Kilner, R. J. Chater, *Solid State Ionics* **2004**, *166*, 89 – 102.

[9] I. Valov, J. Janek, *Solid State Ionics* **2006**, *177*, 1619 – 1624.

[10] S. Kim, S. Wang, X. Chen, Y. L. Yang, N. Wu, A. Igantiev, A. J. Jacobson, B. Abeles, *J. Electrochem. Soc.* **1999**, *147*, 2398 – 2406.

[11] R. A. De Souza, J. A. Kilner, *Solid State Ionics* **1999**, *126*, 153 – 161.

[12] R. Merkle, J. Maier, *Phys. Chem. Chem. Phys.* **2002**, *4*, 4140 – 4148.

[13] J. Maier, *Solid State Ionics* **1998**, *112*, 197 – 228.

[14] J. Maier, *Solid State Ionics* **2000**, *135*, 575 – 588.

[15] J. E. ten Elshof, M. H. R. Lankhorst, H. J. M. Bouwmeester, *J. Electrochem. Soc.* **1997**, *144*, 1060 – 1067.

[16] S. B. Adler, X. Y. Chen, J. R. Wilson, *J. Catal.* **2007**, *245*, 91 – 109.

[17] M. Leonhardt, R. A. De Souza, J. Claus, J. Maier, *J. Electrochem. Soc.* **2002**, *149*, J19 – J26.

[18] M. Leonhardt, J. Jamnik, J. Maier, *Electrochem. Solid-State Lett.* **1999**, *2*, 333 – 335.

[19] J. Jamnik, J. Maier, *Ber. Bunsen-Ges.* **1997**, *101*, 23 – 40.

[20] J. Jamnik, J. Maier, *J. Phys. Chem. Solids* **1998**, *59*, 1555 – 1569.

[21] J. Maier, *J. Am. Ceram. Soc.* **1993**, *76*, 1223 – 1227.

[22] J. Claus, M. Leonhardt, J. Maier, *J. Phys. Chem. Solids* **2000**, *61*, 1199 – 1207.

[23] H. Schmalzried, *Chemical Kinetics of Solids*, VCH, Weinheim, **1995**.

[24] J. Janek, S. Majoni, *Ber. Bunsen-Ges.* **1995**, *99*, 14 – 20.

[25] M. Eiswirth, P. Möller, K. Wetzl, R. Imbihl, G. Ertl, *J. Chem. Phys.* **1989**, *90*, 510 – 521.

[26] H. Meinhard, A Gierer, *J. Cell Sci.* **1974**, *15*, 312 – 346.

[27] S. Busch, U. Schwarz, R. Kniep, *Chem. Mater.* **2001**, *13*, 3260 – 3271.

[28] M. Backhaus-Ricoult, H. Schmalzried, *Ber. Bunsen-Ges.* **1985**, *89*, 1323 – 1330.

[29] R. Waser, T. Baiatu, K.-H. Härdtl, *J. Am. Ceram. Soc.* **1990**, *73*, 1645 – 1653.

[30] S. Rodewald, J. Fleig, J. Maier, *J. Am. Ceram. Soc.* **2000**, *83*, 1969 – 1976.

[31] H. Schmalzried, W. Laqua, *Oxid. Met.* **1981**, *15*, 339 – 353.

[32] M. Martin, *Solid State Ionics* **2000**, *136*, 331 – 337.

[33] E. Kotomin, V. Kuzovkov, *Modern Aspects of Diffusion-controlled Reactions*, Elsevier, Amsterdam, **1996**.

[34] D. E. Mack, S. Wissmann, K.-D. Becker, *Solid State Ionics* **2000**, *135*, 625 – 630.

[35] T. Bieger, J. Maier, R. Waser, *Ber. Bunsen-Ges.* **1993**, *97*, 1098 – 1104.

[36] K. Sasaki, J. Maier, *Phys. Chem. Chem. Phys.* **2000**, *2*, 3055 – 3061.

[37] I. Denk, F. Noll, J. Maier, *J. Am. Ceram. Soc.* **1997**, *80*, 279 – 285.

[38] J. Daniels, K.-H. Härdtl, D. Hennings, R. Wernicke, *Philips Res. Report* **1976**, *31*, 487 – 488.

[39] G. M. Choi, H. L. Tuller, *J. Am. Ceram. Soc.* **1988**, *71*, 201 – 205.

[40] S. Steinsvik, R. Bugge, J. Gjonnes, J. Tafto, T. Norby, *J. Phys. Chem. Solids* **1997**, *58*, 969 – 976.

[41] B. W. Veal, A. P. Paulikas, *Physica C* **1991**, *184*, 321 – 331.

[42] A. Lebon, P. Adler, C. Bernhard, A. V. Boris, A. V. Pimenov, A. Maljuk, C. T. Lin, C. Ulrich, B. Keimer, *Phys. Rev. Lett.* **2004**, *92*, 037202.

[43] Y. Takeda, K. Kanno, T. Takada, O. Yamamoto, M. Takano, N. Nakayama, Y. Bando, *J. Solid State Chem.* **1986**, *63*, 237 – 249.

[44] V. V. Kharton, A. V. Kovalevsky, A. P. Viskup, J. R. Jurado, F. M. Figueiredo, E. N. Naumovich, J. R. Frade, *J. Solid State Chem.* **2001**, *156*, 437 – 444.

[45] Z. P. Shao, W. S. Yang, Y. Cong, H. Dong, J. H. Tong, G. X. Xiong, *J. Membr. Sci.* **2000**, *172*, 177 – 188.

[46] H. J. M. Bouwmeester, *Catal. Today* **2003**, *82*, 141 – 150.

[47] C. Tragut, K.-H. Härdtl, *Sens. Actuators B* **1991**, *4*, 425 – 429.

[48] K. Sahner, R. Moos, *Phys. Chem. Chem. Phys.* **2007**, *9*, 635 – 642.

[49] P. J. Gellings, H. J. M. Bouwmeester, *Catal. Today* **1992**, *12*, 1 – 105.

[50] P. J. Gellings, H. J. M. Bouwmeester, *Catal. Today* **2000**, *58*, 1 – 53.

[51] P. Mars, D. van Krevelen, *Spec. Supp. Chem. Eng.* **1954**, *3*, 54.

[52] P. Kampe, L. Giebeler, D. Samuelis, J. Kunert, A. Drochner, F. Haaß, A. H. Adams, J. Ott, G. Schimanke, T. Buhrmester, M. Martin, H. Fuess, H. Vogel, *Phys. Chem. Chem. Phys.* **2007**, *9*, 3577 – 3589.

[53] J. Fleig, *Annu. Rev. Mater. Res.* **2003**, *33*, 361 – 382.

[54] S. B. Adler, *Chem. Rev.* **2004**, *104*, 4791 – 4843.

[55] R. Metselaar, P. K. Larsen, *J. Phys. Chem. Solids* **1976**, *37*, 599 – 605.

[56] R. A. De Souza, J. A. Kilner, *Solid State Ionics* **1998**, *106*, 175 – 187.

[57] H. Hilgenkamp, J. Mannhart, *Appl. Phys. Lett.* **1998**, *73*, 265 – 267.

[58] C. S. Koonce, M. L. Cohen, J. F. Scooley, W. R. Hosler, E. R. Pfeiffer, *Phys. Rev.* **1967**, *163*, 380 – 390.

[59] K. A. Müller, H. Burkard, *Phys. Rev. B* **1979**, *19*, 3593 – 3602.

[60] N. Setter, R. Waser, *Acta Mater.* **2000**, *48*, 151 – 178.

[61] A. I. Kingon, J.-P. Maria, S. K. Streiffer, *Nature* **2000**, *406*, 1032 – 1038.

[62] P. Padmini, T. R. Taylor, M. J. Lefevre, A. S. Nagra, R. A. York, J. S. Speck, *Appl. Phys. Lett.* **1999**, *75*, 3186 – 3188.

[63] S. Itoh, H. Toki, K. Tamura, F. Kataoka, *Jpn. J. Appl. Phys.* **1999**, *38*, 6387 – 6391.

[64] J. G. Mavroides, J. A. Kafalas, D. F. Kolesar, *Appl. Phys. Lett.* **1976**, *28*, 241 – 243.

[65] J. M. Lehn, J. P. Sauvage, R. Ziessel, *Nouv. J. Chim.* **1980**, *4*, 623 – 627.

[66] H. Kato, A. Kudo, *J. Phys. Chem. B* **2002**, *106*, 5029 – 5034.

[67] O. A. Marina, N. L. Canfield, J. W. Stevenson, *Solid State Ionics* **2002**, *149*, 21 – 28.

[68] A. Ovalle, J. C. Ruiz-Morales, J. Canales-Vasquez, D. Marrero-Lopez, J. T. S. Irvine, *Solid State Ionics* **2006**, *177*, 1997 – 2003.

[69] J. B. Goodenough, *Rep. Prog. Phys.* **2004**, *67*, 1915 – 1993.

[70] J. Maier, *Angew. Chem.* **1993**, *105*, 333 – 354; *Angew. Chem. Int. Ed. Engl.* **1993**, *32*, 313 – 335.

[71] J. Maier, *Physical Chemistry of Ionic Materials*, Wiley, Chichester, **2004**.

[72] F. A. Kröger, *Chemistry of Imperfect Crystals*, North-Holland, Amsterdam, **1964**.

[73] K. Sasaki, J. Maier, *J. Appl. Phys.* **1999**, *86*, 5422 – 5433; K. Sasaki, J. Maier, *J. Appl. Phys.* **1999**, *86*, 5434 – 5443.

[74] The perovskite structure $ABO_{3-\delta}$ is an extremely versatile crystal structure which forms when the sum of the cation charges is 6 and the ionic radii fulfill the Goldschmidt criterion $(r_A + r_O)/[\sqrt{2}(r_B + r_O)] \approx 1$. It can accommodate an astonishingly large number of dopants on the A as well as on the B site, often in concentrations of a few percent. In some cases, very high concentrations up to a full solid solution series such as $Sr(Fe_xTi_{1-x})O_{3-\delta}$ are possible. Negative dopants are at least partially compensated by the formation of mobile oxygen vacancies. $SrTiO_3$ with positive dopants nominally has an excess of oxygen, but oxygen interstitials cannot be accommodated in the dense perovskite structure. Charge compensation is (partly) realized by cation vacancies with low mobility; therefore, these materials are often not fully equilibrated.

[75] R. Moos, W. Menesklou, K.-H. Härdtl, *Appl. Phys. A* **1995**, *61*, 389 – 395.

[76] C. Wagner, W. Schottky, *Z. Phys. Chem. Abt. B* **1930**, *11*, 163 – 210.

[77] A. R. Allnatt, A. B. Lidiard, *Atomic Transport in Solids*, Cambridge University Press, Cambridge, **1993**.

[78] I. Denk, W. Münch, J. Maier, *J. Am. Ceram. Soc.* **1995**, *78*, 3265–3272.

[79] N. H. Chan, R. K. Sharma, D. M. Smyth, *J. Electrochem. Soc.* **1981**, *128*, 1762–1781.

[80] R. Waser, T. Bieger, J. Maier, *Solid State Commun.* **1990**, *76*, 1077–1081.

[81] R. Waser, *J. Am. Ceram. Soc.* **1991**, *74*, 1934–1940.

[82] M. Fleischer, H. Meixner, C. Tragut, *J. Am. Ceram. Soc.* **1992**, *75*, 1666–1668.

[83] E. S. Kirkpatrick, K. A. Müller, R. S. Rubins, *Phys. Rev.* **1964**, *135*, A86–A90.

[84] R. Merkle, J. Maier, *Phys. Chem. Chem. Phys.* **2003**, *5*, 2297–2303.

[85] J. Jamnik, J. Maier, S. Pejovnik, *Solid State Ionics* **1995**, *75*, 51–58.

[86] R. Moos, K.-H. Härdtl, *J. Am. Ceram. Soc.* **1997**, *80*, 2549–2562. Since the formation of Ti vacancies in $SrTiO_3$ is energetically unfavorable, the partial Schottky reaction $O_O^x + Sr_{Sr}^x \rightleftharpoons V_O^{\bullet\bullet} + V_{Sr}'' + SrO_{surface}$ is the relevant reaction for cation vacancy formation and changes in Sr/Ti ratio.

[87] When $SrTiO_3$ is donor-doped, for example, by introducing $La_{Sr}^\bullet$ or $Nb_{Ti}^\bullet$ defects, the type of the predominantly compensating defect depends on the pO_2: e′ will dominate in the low pO_2 regime, and cation vacancies at high pO_2.[86] The low cation mobility[146–149] will require extremely long equilibration times, and secondary phases will be involved as strontium sources/sinks.[88,89]

[88] A. Gunhold, K. Gömann, L. Beuermann, M. Frerichs, G. Borchardt, V. Kempter, W. Maus-Friedrichs, *Surf. Sci.* **2002**, *507*, 447–452.

[89] R. Meyer, K. Szot, R. Waser, *Ferroelectrics* **1999**, *224*, 323–329.

[90] J. Maier, *Angew. Chem.* **1993**, *105*, 558–571; *Angew. Chem. Int. Ed. Engl.* **1993**, *32*, 528–542.

[91] J. Maier, *Z. Anorg. Allg. Chem.* **2005**, *631*, 433–442.

[92] J. O'M. Bockris, A. K. N. Reddy, M. Gamboa-Aldeco, *Modern Electrochemistry 2A*, Kluwer, New York, **2000**.

[93] Because of the different definitions of $\Re$ and $j = \Re\Delta x$, $\bar{k}_R^\delta$ in Equation (15) and $\bar{k}^\delta$ in Equation (16) differ by a factor Δx corresponding to the spatial distance involved in the reaction. For the sake of simplicity, this factor is absorbed in the other constant prefactors and not mentioned explicitly further in the manuscript.

[94] J. Jamnik, J. Maier, *Phys. Chem. Chem. Phys.* **2001**, *3*, 1668–1678.

[95] http://www.fkf.mpg.de/maier/downloads.html.

[96] In the steady state, all reaction rates are of course identical; "slow" and "fast" refers to the exchange rate of the respective step.

[97] In principle, $\Delta\phi_{surf}$ varies with the degree of coverage by charged adsorbates as a function of pO_2 and T, but this contribution is negligible for small coverages. Since most defects have rather small pO_2 dependencies, their possible contribution to $\Delta\phi_{surf}$ is also expected to change only slightly. Thus pO_2-independent contributions to $\Delta\phi_{surf}$, for example, from dopant segregation can be assumed to dominate and $\Delta\phi_{surf}$ is approximately constant. This assumption is in line with the finding of an almost pO_2- and temperature-independent value of $\Delta\phi_{gb}$ for Fe-doped $SrTiO_3$.[126]

[98]
$$K_{pre} = \frac{[O_2^-][h^\bullet]}{pO_2} \Rightarrow \frac{\delta[O_2^-]}{[\hat{O}_2^-]} \equiv \frac{[O_2^-]\text{-}[\hat{O}_2^-]}{[\hat{O}_2^-]} = \left(\frac{[\hat{h}^\bullet]-[h^\bullet]}{[h^\bullet][\hat{h}^\bullet]}\right)[\hat{h}^\bullet] \approx \frac{-\delta[h^\bullet]}{[\hat{h}^\bullet]};$$

$$K_{bg} = [e'][h^\bullet] \Rightarrow \frac{-\delta[h^\bullet]}{[\hat{h}^\bullet]} = \frac{\delta[e']}{[\hat{e}']};\text{analogous for } \frac{\delta[O_2^{2-}]}{[\hat{O}_2^{2-}]}.$$

[99] $1/2O_2 + V_O^{\bullet\bullet} \rightleftharpoons O_O^x + 2h^\bullet \Rightarrow \partial\mu_O = -\partial\mu_{V_O^{\bullet\bullet}} + 2\partial\mu_{h^\bullet}$. (the chemical potential of the regular oxide ions O_O^x is approximately constant)$\Rightarrow$

$$\frac{\partial\mu_O}{\partial c_O} = \frac{\partial\mu_{V_O^{\bullet\bullet}}}{\partial[V_O^{\bullet\bullet}]} + 2\frac{\partial\mu_{h^\bullet}}{\partial[h^\bullet]}\frac{\partial[h^\bullet]}{\partial c_O} = RT\left(\frac{1}{[V_O^{\bullet\bullet}]} + \frac{2}{[h^\bullet]}\frac{\partial[h^\bullet]}{\partial c_O}\right).$$ For dilute defect concentrations, $\partial\mu_i/\partial c_i = RT/c_i$. Inserting $\partial c_O = -\partial[V_O^{\bullet\bullet}] = \partial[h^\bullet]/2$ (the annihilation of one $V_O^{\bullet\bullet}$ creates two $h^\bullet$ in absence of redox-active ions) leads to $\frac{\partial\mu_O}{\partial c_O} = RT\left(\frac{1}{[V_O^{\bullet\bullet}]} + \frac{4}{[h^\bullet]}\right)$. In the presence of redox-active centers $2\partial[V_O^{\bullet\bullet}] + \partial[h^\bullet] = \partial[Fe'_{Ti}] = -\partial[Fe_{Ti}^x]$ holds (for trapping at iron according to $Fe_{Ti}^x \rightleftharpoons Fe'_{Ti} + h^\bullet$). Thus $\frac{\partial[h^\bullet]}{\partial[V_O^{\bullet\bullet}]} = \frac{-2\partial[h^\bullet]}{\partial[h^\bullet] + \partial[Fe_{Ti}^x]} \equiv -2\chi$ and

$$\frac{\partial\mu_O}{\partial c_O} = RT\left(\frac{1}{[V_O^{\bullet\bullet}]} + \chi\frac{4}{[h^\bullet]}\right).$$ "Free" ($h^\bullet$) and "trapped" holes (Fe_{Ti}^x) together form a conservative ensemble[21] where χ is the differential change of free hole concentration upon concentration change if this ensemble (more precisely χ^{-1} should be termed trapping factor).

[100] J. Maier, *Solid State Ionics* **2004**, *173*, 1–8.

[101] R. Merkle, R. A. De Souza, J. Maier, *Angew. Chem.* **2001**, *113*, 2184–2187; *Angew. Chem. Int. Ed.* **2001**, *40*, 2126–2129.

[102] S. F. Wagner, C. Warnke, W. Menesklou, C. Argirusis, T. Damjanovic, G. Borchardt, E. Ivers-Tiffee, *Solid State Ionics* **2006**, *177*, 1607–1612.

[103] T. Sano, D. M. Saylor, G. S. Rohrer, *J. Am. Ceram. Soc.* **2003**, *86*, 1933–1939.

[104] M. Kawasaki, K. Takahashi, T. Maeda, R. Tsuchiya, M. Shinohara, O. Ishiyama, T. Yoshimoto, H. Koinuma, *Science* **1994**, *266*, 1540–1542.

[105] Y. Matsumoto, T. Ohsawa, R. Takahashi, H. Koinuma, *Thin Solid Films* **2005**, *486*, 11–14.

[106] M. Che, A. J. Tench, *Adv. Catal.* **1982**, *31*, 77–133; M. Che, A. J. Tench, *Adv. Catal.* **1982**, *32*, 1–148.

[107] A. Rothschild, Y. Komem, *Sens. Actuators B* **2003**, *93*, 362–369.

[108] A. Gurlo, *ChemPhysChem* **2006**, *7*, 2041–2052.

[109] M. Leonhardt, PhD thesis, University of Stuttgart, **1999**.

[110] R. A. De Souza, J. Zehnpfenning, M. Martin, J. Maier, *Solid State Ionics* **2005**, *176*, 1465–1471.

[111] R. A. De Souza, M. Martin, unpublished results.

[112] R.-V. Wang, P. C. McIntyre, *J. Appl. Phys.* **2005**, *97*, 023508.

[113] J. Maier, unpublished results.

[114] C. Wagner, *Z. Elektrochem.* **1956**, *60*, 4–7.

[115] I. Yokota, *J. Phys. Soc. Jpn.* **1961**, *16*, 2213–2223.

[116] Nernst–Einstein relation: $D_i = RT\sigma_i/(z_i^2F^2c_i)$. W. Nernst, *Z. Phys. Chem.* **1888**, *2*, 613–637.

[117] T. Ishigaki, S. Yamauchi, K. Kishio, J. Mizusaki, K. Fueki, *J. Solid State Chem.* **1988**, *73*, 179–187.

[118] J. A. Kilner, R. A. De Souza, I. C. Fullarton, *Solid State Ionics* **1996**, *86*, 703–709.

[119] K. Sasaki, J. Maier, *Solid State Ionics* **2000**, *134*, 303–321.

[120] C.-J. Shin, H.-I. Yoo, *Solid State Ionics* **2007**, *178*, 1089–1094.

[121] R. Merkle, J. Maier, K.-D. Becker, M. Kreye, *Phys. Chem. Chem. Phys.* **2004**, *6*, 3633–3638.

[122] J. Maier, J. Jamnik, M. Leonhardt, *Solid State Ionics* **2000**, *129*, 25–32.

[123] M. Vollmann, R. Hagenbeck, R. Waser, *J. Am. Ceram. Soc.* **1997**, *80*, 2301–2314.

[124] A. Tschöpe, *Solid State Ionics* **2001**, *139*, 267–280.

[125] S. Kim, J. Maier, *J. Am. Ceram. Soc.* **2002**, *149*, J73–83.

[126] R. A. De Souza, J. Fleig, J. Maier, O. Kienzle, Z. Zhang, W. Sigle, M. Rühle, *J. Am. Ceram. Soc.* **2003**, *86*, 922–928.

[127] For the cases discussed here, impedance spectra can be modeled by equivalent circuits comprising resistors R and

capacitors C (or constant phase elements CPE, which correspond to a certain distribution of capacitances). A sample exhibiting only bulk conductivity shows one semicircle in the plot of imaginary versus real part of the impedance (its peak frequency is given by $\omega^{-1} = RC =$ relaxation time of the process), and can be represented by a parallel R–C combination. The presence of blocking grain boundaries leads to an additional semicircle at low frequencies described by an additional R'–C' or R'–CPE′ combination (R' = grain boundary resistance because of charge carrier depletion, C' or CPE' = grain boundary capacitance $\gg$ bulk capacitance, because the ratio of grain size to space–charge zone thickness enters the capacitor equation; see reference [139]).

[128] X. Guo, J. Fleig, J. Maier, *J. Electrochem. Soc.* **2001**, *148*, J50–J53.

[129] S. Kim, J. Fleig, J. Maier, *Phys. Chem. Chem. Phys.* **2003**, *5*, 2268–2273.

[130] J. Jamnik, J. Maier, *J. Phys. Chem. Solids* **1998**, *59*, 1555–1569.

[131] M. Vollmann, R. Waser, *J. Am. Ceram. Soc.* **1994**, *77*, 235–243.

[132] G. E. Pike, C. H. Seager, *J. Appl. Phys.* **1979**, *50*, 3414–3422.

[133] S. M. Sze, *Semiconductor Devices*, Wiley, New York, **1985**.

[134] This expression is valid as long as no inversion of the charge-carrier concentrations close to the grain boundary core occurs, that is, as long as $[h^\bullet] > [e']$; see reference [135].

[135] S. Rodewald, J. Fleig, J. Maier, *J. Appl. Phys.* **2000**, *87*, 2372–2381.

[136] D. C. Grahame, *Chem. Rev.* **1947**, *41*, 441–501.

[137] Z. Zhang, W. Sigle, R. A. De Souza, W. Kurtz, J. Maier, M. Rühle, *Acta Mater.* **2005**, *53*, 5007–5015.

[138] O. Kienzle, M. Exner, F. Ernst, *Phys. Status Solidi A* **1998**, *166*, 57–71.

[139] S. Rodewald, J. Fleig, J. Maier, *J. Am. Ceram. Soc.* **2001**, *84*, 521–530.

[140] M. Fujimoto, Y.-M. Chiang, A. Roshko, W. D. Kingery, *J. Am. Ceram. Soc.* **1985**, *68*, C300–303.

[141] W. Heywang, *Solid State Electr.* **1961**, *3*, 51–58.

[142] J. Maier, *Nat. Mater.* **2005**, *4*, 805–815.

[143] P. Balaya, J. Jamnik, J. Fleig, J. Maier, *Appl. Phys. Lett.* **2006**, *88*, 062109.

[144] I. Kaur, Y. Mishin, W. Gust, *Fundamentals of Grain and Interphase Boundary Diffusion*, Ziegler, Stuttgart, **1995**.

[145] D. Gryaznov, J. Fleig, J. Maier, *Solid State Ionics* **2006**, *177*, 1583–1586.

[146] R. Meyer, R. Waser, J. Helmbold, G. Borchardt, *Phys. Rev. Lett.* **2003**, *90*, 105901.

[147] K. Gömann, G. Borchardt, A. Gunhold, W. Maus-Friedrichs, H. Baumann, *Phys. Chem. Chem. Phys.* **2004**, *6*, 3639–3644.

[148] K. Gömann, G. Borchardt, M. Schulz, A. Gömann, W. Maus-Friedrichs, B. Lesage, O. Kaitasov, S. Hoffmann-Eifert, T. Schneller, *Phys. Chem. Chem. Phys.* **2005**, *7*, 2053–2060.

[149] W. Preis, W. Sitte, *Solid State Ionics* **2006**, *177*, 3093–3098.

[150] A. Rothschild, W. Menesklou, H. L. Tuller, E. Ivers-Tiffee, *Chem. Mater.* **2006**, *18*, 3651–3659.

[151] H. D. Zhou, J. B. Goodenough, *J. Solid State Chem.* **2004**, *177*, 1952–1957.

[152] R. Merkle, J. Maier, unpublished results.

[153] R. A. Evarestov, S. Piskunov, E. A. Kotomin, G. Borstel, *Phys. Rev. B* **2003**, *67*, 064101.

[154] R. Moos, W. Menesklou, H. J. Schreiner, K.-H. Härdtl, *Sens. Actuators B* **2000**, *67*, 178–183.

[155] J. R. Jurado, M. T. Colomer, J. R. Frade, *Solid State Ionics* **2001**, *143*, 251–257.

[156] R. Merkle, J. Maier, *Solid State Ionics* **2006**, submitted.

[157] W. Preis, E. Bucher, W. Sitte, *Solid State Ionics* **2004**, *175*, 393–397.

[158] R. Merkle, J. Maier, *Top. Catal.* **2006**, *38*, 141–145.

[159] K. Q. Huang, J. B. Goodenough, *J. Electrochem. Soc.* **2001**, *148*, E203–E214.

[160] G. Kim, S. Wang, A. J. Jacobson, Z. Yuan, W. Donner, C. L. Chen, L. Reimus, P. Brodersen, C. A. Mims, *Appl. Phys. Lett.* **2006**, *88*, 024103.

[161] T. Kawada, J. Suzuki, M. Sase, A. Kamai, K. Yashiro, Y. Nigara, J. Mizusaki, K. Kawamura, H. Yugami, *J. Electrochem. Soc.* **2002**, *149*, E252–E259.

[162] J. R. Wilson, M. Sase, T. Kawada, S. B. Adler, *Electrochem. Solid-State Lett.* **2007**, *10*, B81–B86.

[163] T. Ishigaki, S. Yamauchi, K. Kishio, J. Mizusaki, K. Fueki, *J. Solid State Chem.* **1988**, *73*, 179–187.

[164] C. A. Mims, N. Bayani, A. J. Jacobson, P. A. W. van der Heide, *Solid State Ionics* **2005**, *176*, 319–323.

[165] R. A. De Souza, *Phys. Chem. Chem. Phys.* **2006**, *8*, 890–897.

[166] M. Vracar, R. Merkle, J. Maier, unpublished results.

[167] The observed fractional reaction orders for CH_4 and O_2 result from a delicate balance of three competing processes, which all affect the concentrations of adsorbed oxygen species and thus the CH_4 oxidation rate: 1) chemisorption of oxygen species from the gas phase, 2) incomplete equilibration of chemisorbed oxygen species with the bulk defects, 3) removal of chemisorbed oxygen species by reaction with CH_4.

[168] R. Waser, *Ber. Bunsen-Ges.* **1986**, *90*, 1223–1230.

[169] S. Stotz, C. Wagner, *Ber. Bunsen-Ges.* **1966**, *70*, 781–788.

[170] K.-D. Kreuer, S. Adams, W. Münch, A. Fuchs, U. Klock, J. Maier, *Solid State Ionics* **2001**, *145*, 295–306.

[171] J. H. Yu, J. S. Lee, J. Maier, *Phys. Chem. Chem. Phys.* **2005**, *7*, 3560–3564.

[172] J. H. Yu, J. S. Lee, J. Maier, *Angew. Chem.* **2007**, *119*, 9150–9152; *Angew. Chem. Int. Ed.* **2007**, *46*, 8992–8994.

[173] N. Barsan, U. Weimar, *J. Electroceram.* **2001**, *7*, 143–167.

[174] G. Blaustein, M. S. Castro, C. M. Aldao, *Sens. Actuators B* **1999**, *55*, 33–37.

[175] B. Kamp. R. Merkle, J. Maier, *Sens. Actuators B* **2001**, *77*, 534–542.

[176] D. Gryaznov, J. Fleig, J. Maier, *Solid State Sci.* **2007**, submitted .

[177] K. Reuter, D. Frenkel, M. Scheffler, *Phys. Rev. Lett.* **2004**, *93*, 116105.

[178] K. Honkala, A. Hellman, I. N. Remediakis, A. Longadottir, A. Carlsson, S. Dahl, C. H. Christensen, J. K. Norskov, *Science* **2005**, *307*, 555–558.

[179] X. Wu, A. Selloni, M. Lazzeri, S. K. Nayak, *Phys. Rev. B* **2003**, *68*, 241402.